REDUCED-ORDER MODELING AND DESIGN OPTIMIZATION OF METAL-PCM COMPOSITE HEAT EXCHANGERS

A Thesis

Submitted to the Faculty

of

Purdue University

by

Karan N. Gohil

In Partial Fulfillment of the

Requirements for the Degree

of

Master of Science

May 2020

Purdue University

West Lafayette, Indiana

THE PURDUE UNIVERSITY GRADUATE SCHOOL

STATEMENT OF THESIS APPROVAL

Dr. Neera Jain, Chair

School of Mechanical Engineering

Dr. Amy Marconnet

School of Mechanical Engineering

Dr. George Chiu

School of Mechanical Engineering

Dr. Patrick Shamberger

Department of Material Science and Engineering, Texas A&M University

Approved by:

Dr. Nichole L. Key

Head of the School Graduate Program

To my family, friends and teachers.

ACKNOWLEDGMENTS

I would like to express my deepest gratitude to my advisor, Dr. Neera Jain, for her invaluable guidance and support during the last two years.

I thank Dr. Patrick Shamberger, for his useful feedback throughout the collaboration. I thoroughly enjoyed working with Michael Deckard and I am thankful for their contributions during the course of this project.

I would also like to thank the members of Jain Research Lab for their constant guidance on navigating the graduate coursework and research, as well as for enriching my experience at Purdue through their friendship.

Lastly, I would like to acknowledge the support of the Center of Excellence for Integrated Thermal Management of Aerospace Vehicles for the opportunity to engage in its important research and the Herrick Laboratories for providing me opportunities to network with great researchers and industry members.

TABLE OF CONTENTS

LIST OF TABLES

LIST OF FIGURES

Figure Page

Figure Page

Figure Page

SYMBOLS

A	area of contact, m^2
c_p	specific heat, J/K
D	hydraulic diameter, m
d	depth of thermal energy storage module, m
E_f	energy lost by flowing fluid, J
h	height, m
J	cost function
l	length of a control volume, m
L	length of the fluid channel, m
L_{char}	characteristic length of a channel, m
L_{fus}	latent heat of fusion, J/kg
m	mass, kg
$\dot{m}$	mass flow rate, kg/s
N	number of thermal energy storage modules
n	number of layers or sections, m
$\dot{Q}$	rate of change of energy, W
R_j^i	thermal resistance between ith and jth element, K/W
T	temperature, K
α	convection coefficient, W/m^2K
μ	viscosity, kg/ms
ϕ	metal fraction in composite phase change material layer
ρ	density, kg/m^3

Subscripts

c	entire composite phase change material
$ci-$	bottom half of ith composite phase change material layer
$ci+$	top half of ith composite phase change material layer
ci	entire ith composite phase change material layer
f	fluid
in	inlet
L	parallel to fluid flow
m	melting point
O	overall system
out	outlet
p	entire metal plate or metal tube
$p-$	bottom half of metal plate or metal tube
$p+$	top half of metal plate or metal tube
r	perpendicular to fluid flow

Superscripts

ci	ith sub-layer of CPCM
f	fluid
j	element index
L	parallel to fluid flow
p	metal plate/tube
r	perpendicular to fluid flow

ABBREVIATIONS

CFD	computational fluid dynamics
CPCM	composite phase change material
HX	heat exchanger
PCM	phase change material
TES	thermal energy storage

ABSTRACT

Gohil, Karan N. M.S., Purdue University, May 2020. Reduced-order Modeling And Design Optimization Of Metal-PCM Composite Heat Exchangers. Major Professor: Neera Jain, School of Mechanical Engineering.

Thermal energy storage (TES) modules are specifically designed to respond to transient thermal loading. Their dynamic response depends on the overall structure of the module, including module geometry and dimensions, the internal spatial distribution of phase change material (PCM) and conductive heat-spreading elements, and the thermophysical properties of the different materials composing the module. However, due to the complexity of analyzing a system's dynamic thermal response to transient input signals, optimal design of a TES module for a particular application is challenging. Conventional design approaches are limited by (1) the computational cost associated with high fidelity simulation of heat transfer in nonlinear systems undergoing a phase transition and (2) the lack of model integration with robust optimization tools. To overcome these challenges, I derive reduced-order dynamic models of two different metal-PCM composite TES modules and validate them against a high fidelity CFD model. Through simulation and validation of both turbulent and laminar flow cases, I demonstrate the accuracy of the reduced-order models in predicting, both spatially and temporally, the evolution of the dynamic model states and other system variables of interest, such as PCM melt fraction. The validated models are used to conduct univariate and bivariate parametric studies to understand the effects of various design parameters on different performance metrics. Finally, a case study is presented in which the models are used to conduct detailed design optimization for the two HX geometries.

1. INTRODUCTION

Transient heating in high power electronic and optical systems results in ephemeral temperature rises which can damage components. Given that a cooling system's size and complexity generally scales with the required heat rejection rate, thermal energy storage (TES) heat exchangers (HX), or modules, which commonly utilize phase change materials (PCMs) to absorb heat due to the latent heat of melting, offer a compact and efficient alternative to buffer thermal transients. TES modules are specifically designed to operate during thermal transients, where the dynamic thermal response of the module under a transient thermal load is of primary interest. This dynamic response depends on the overall structure of the module, including module geometry and dimensions, the internal spatial distribution of PCM and conductive heat-spreading elements, and the thermophysical properties of the different materials composing the module. These structural attributes interact with a transient heat pulse and affect the dynamic thermal response of the module. However, due to the complexity of analyzing a system's dynamic thermal response to transient input signals, optimal design of a TES module for a particular application is challenging. Traditional approaches to design are limited by (1) the computational cost associated with high fidelity simulation of heat transfer in nonlinear systems undergoing a phase transition and by (2) the lack of model integration with robust optimization tools.

1.1 Literature Review

Several researchers have modeled TES modules with integrated PCM using CFD software [1–4], while others have used reduced-order modeling techniques [5–11]. Ta-

ble 1.1 summarizes work on metal heat exchangers with embedded or integrated PCM, to be referred to as composite phase change material (CPCM) TES modules from here onward. The authors of [5] present a reduced-order model for a cylindrical tube type heat exchanger having a layer of pure PCM (without any metal fins in the layer) surrounding the fluid channel. The authors use a grid of 51 $\times$ 19 (length $\times$ axial direction) to simulate the reduced-order model and present a parametric study where they assess the effects of the outer radius of the PCM layer, the mass flow rate of the working fluid, and the inlet temperature of the working fluid on performance metrics including the energy stored in the PCM layer, the working fluid outlet temperature, the rate of heat transfer between the working fluid and the PCM layer, and the melt fraction of PCM. The theoretical model is used to predict the transient behavior of the cylindrical tube HX by taking into account the effect of natural convection of the melt layer of the PCM. However, the authors do not discuss the use of numerical optimization techniques for design optimization using their model. Similarly, the authors of [8] develop a reduced-order model for a cylindrical tube heat exchanger with a pure PCM layer surrounding the fluid channel. They simulate the reduced-order model using a grid of 100 $\times$ 40 and study the effects of fluid temperature and fluid inlet mass flow rate on the PCM melting time. In [9], the authors develop a CFD model of a flat plate metal-PCM heat exchanger and assume a uniform heat flux condition to study the effect of melt convection on the thermal performance of the heat exchanger. The authors consider a grid of size 5 $\times$ 23 for the PCM section and a grid of 3 $\times$ 23 for the metal fin. Similarly, the authors of [11] develop a reduced-order model for a PCM-based pin fin heat sink. They also use a uniform heat flux condition and perform a design optimization that maximizes the heat sink operation time using the reduced-order model. One limitation of these models is that integration of the TES fluid channel in a system-level simulation may not necessarily result in a

uniform heat flux across the fluid-metal interface, thereby precluding the model from being readily integrated with other thermal-fluid components and architectures. The authors of [3] develop a CFD model for a pin fin matrix heat sink and train a neural network to find input-output correlations between the design parameters and the performance metrics. The performance metrics considered in the paper are charging and discharging time of the heat sink. However, one limitation of this work is that using a neural network to find an optimal solution does not guarantee a global optimum. Moreover, they use a constant power supply to melt the CPCM layer; in other words, the dynamics of the heat transfer between the fluid channel and metal separator are not modeled.

In summary, little work has been done to consider a reduced-order model of a metal-PCM heat exchanger for a system-level integration in a dynamic optimization problem that optimizes component design for dynamic performance metrics. Similarly, no work considers spatial variation of metal fraction within the CPCM layer as a parameter for a dynamic optimization problem.

1.2 Research Contribution

In this thesis, I derive and validate a reduced-order dynamic model of a thermal energy storage module for the purpose of design optimization with potential for integration into larger thermal system architectures. I specifically model a heat exchanger with PCM embedded between closely spaced metal fins, and adapt the model for two common HX geometries—an extended flat plate HX and a cylindrical tube HX. The validation is conducted against high-fidelity CFD models created in ANSYS Fluent for the same geometries. I explicitly assess the validity of each approximation that was made in the reduced-order model to improve overall computational efficiency, through a series of comparative validation runs. Through simulation and validation

of both turbulent and laminar flow cases, I demonstrate the accuracy of the reduced-order model in predicting, both spatially and temporally, the evolution of the dynamic model states and other system variables of interest, such as critical heat fluxes. The validated models are then exercised for the purpose of module design, both through a set of parametric studies as well as numerical optimization considering several design variables at once.

Table 1.1. : Literature review summary

	Experimental Validation	CFD Model	Reduced Order Model	System Level Integration	Dynamic Optimization	Spatial Variation of Metal Fraction
Lacroix et al. (1993) [5]	X		X	X		
Trp et al. (2006) [6]	X		X	X		
Nagose et al. (2008) [7]			X		X	
Wang et al. (2008) [1]	X	X				
Medrano et al. (2009) [12]	X					
Tao and He (2011) [8]			X	X		
Saha and Dutta (2011) [9]			X		X	
Hosseinizadeh et al. (2011) [2]	X	X			X	
Tao et al. (2014) [10]			X	X		
Srikanth et al. (2015) [3]	X	X			X	
Pakrouh et al. (2015) [11]	X		X		X	
Srivatsa et al. (2016) [4]	X	X			X	
Srikanth and Balaji (2017) [13]	X				X	

1.3 Organisation of Thesis

The remainder of the thesis is organized as follows. In Section 2, I present the governing equations of the reduced-order CPCM HX model. In Section 3, I discuss the high fidelity model used as a benchmark for validation and present validation results for both laminar and turbulent flow regimes for both the geometries. In Section 4, I present a parametric study using the reduced-order model to explore the effect of individual design variables on performance metrics of interest. In Section 5, I demonstrate the use of the model component design optimization using numerical optimization techniques. Then, I conclude the thesis in Section 6.

2. REDUCED-ORDER MODEL

A reduced-order model for two different geometries of metal-PCM heat exchangers are derived in this chapter.

2.1 System Description

Here, two heat exchanger geometries are considered: cylindrical tube and extended plate. Both heat exchangers (HXs) include a heat-transfer fluid channel surrounded by a CPCM layer. The cylindrical heat exchanger geometry consists of a single cylindrical fluid channel surrounded by a metal wall, which is in turn surrounded by a composite metal fin/PCM material structure in a cylindrical configuration, as shown in Figure 2.1. The metal fins, of constant thickness, extend perpendicular towards the axial direction of the fluid channel, separating channels of PCM material.

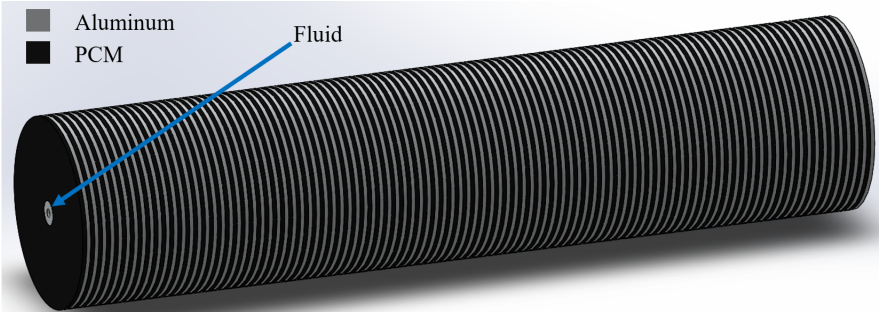

Figure 2.1. : Cylindrical tube simulation geometry with metal fins and PCM embedded between the metal fins.

The extended flat-plate heat exchanger geometry consists of a flat rectangular channel projecting infinitely out of the plane, between two flat metal walls, which are in turn surrounded by two flat slabs of composite metal fin/PCM material structures

as shown in Figure 2.2. Both heat exchangers have a single inlet and outlet for carrying the working fluid, which is assumed to be water in this thesis. The pipe and plate walls are composed of aluminum. The CPCM layer is composed of aluminum fins fused to either the cylindrical tube or the flat plate for the appropriate geometry with PCM material filling the space between adjacent fins. The effective volume fraction of PCM in the CPCM layer is calculated as the ratio of the axial thickness of each PCM layer, to the axial pitch (length from the edge of an aluminum fin to the identical edge of the next aluminum fin).

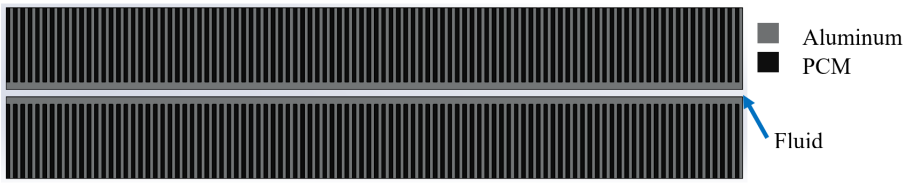

Figure 2.2. : Extended plate simulation geometry showing metal fins and PCM embedded between the metal fins.

2.2 Modeling Approximations

The following approximations were made while deriving the dynamic reduced-order model for the two heat exchanger geometries.

1. **Use of empirical heat transfer correlations.** Heat transfer between the fluid channels and the metal wall or tube can be derived from empirical heat transfer correlations, given knowledge of the fluid flow conditions and channel geometry.

2. **Use of effective composites properties.** Rather than treat the composite PCM layer (which is composed of closely inter-spaced metal fins and PCM layers) as two separate materials, with heat transfer from one to the other, I adopt an 'effective medium approximation' and derive material properties from the

volume fraction of the phases present. This approximation has previously been demonstrated to hold well if the spacing between the conductive components is below a critical length scale (< 1 mm) [14].

3. **Control volume discretization.** The properties and states of a given control volume are constant spatially within that control volume (i.e. lumped) and the entire control volume can be described by a point at the center of that control volume. The selection of the appropriate number of vertical and axial control volumes represents a trade-off between computational complexity and model accuracy.

4. **Negligible gravitational effects in PCM layer.** There is no convective heat transfer within the liquid PCM due to buoyancy-driven convection (i.e., gravitational effects are ignored). This approximation generally holds when: 1) the rate of conductive heat transfer is high, due to the large volume fraction of conductive metal, and 2) convection within the fluid volume is constrained due to the close spacing of the lamellar fins [15].

In addition to these four major approximations, I assume that the fluid is incompressible and that the outer boundary layer of the heat exchanger volume is perfectly adiabatic.

2.3 Governing Equations

For the extended plate heat exchanger, the plane through the axis of the fluid channel parallel to the flow, and into the plane (of page), divides the geometry into two symmetrical halves as shown in Figure 2.3. The plane is assumed to be an adiabatic boundary and using the finite volume method, the problem is defined using the geometry shown in Figure 2.4.

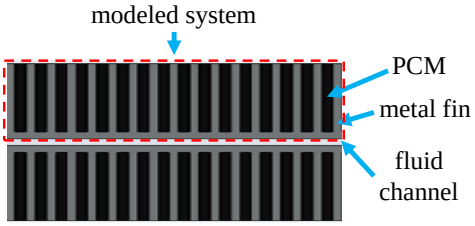

Figure 2.3. : Extended plate simulation geometry showing the geometry considered to develop a reduced-order model using the finite volume method.

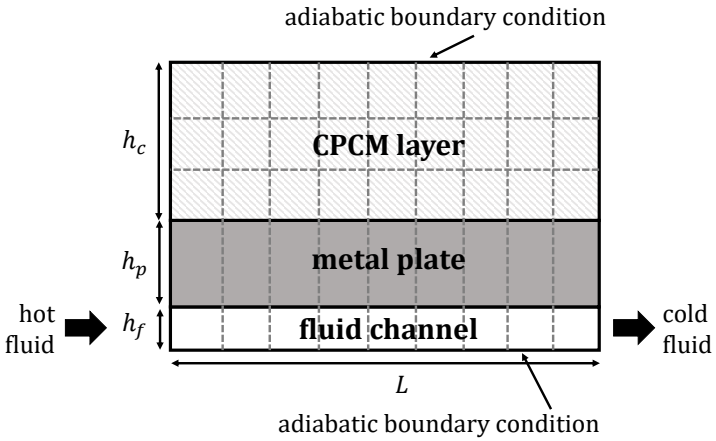

Figure 2.4. : Reduced-order modeling schematic of the flat plate heat exchanger showing the control volumes of the fluid channel, the metal plate and the CPCM layer.

For the cylindrical tube HX, the finite volume method is used to divide the geometry into different sections of the tube along the fluid flow and to divide the CPCM layer geometry into different sub-layers stacked on each other as shown in Figure 2.5.

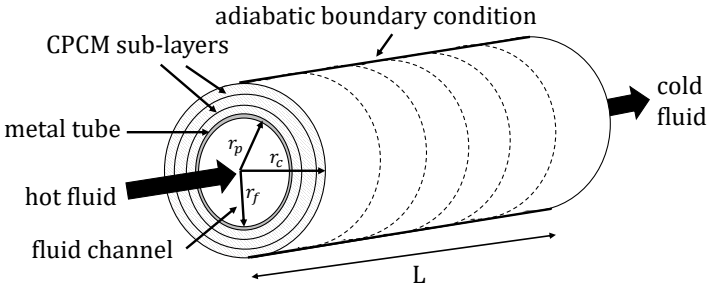

Figure 2.5. : Reduced-order modeling schematic of the cylindrical tube heat exchanger showing the control volumes of the fluid channel, the metal tube and the CPCM layer.

2.3.1 Model Derivation

The governing equations for the reduced-order model for the two geometries are derived by applying mass and energy conservation to each control volume. The model equations are of the same form for the two geometries, with the only exception being the way in which the different thermal resistance values are calculated. Therefore, the model equations derived below are valid for *both* the geometries, the extended flat plate geometry and the cylindrical tube geometry.

Equation 2.1 describes the rate of change of energy contained within the fluid flowing through the fluid channel as shown in Figure 2.6. Here, $\dot{Q}_j^f$ represents the rate of change of energy contained within the jth control volume of the fluid, $\dot{Q}_j^{p\rightarrow f}$ represents the rate of energy flow from the metal plate/tube to the fluid control volume and $\dot{Q}_j^{flow}$ represents the rate of energy flow to the fluid control volume due to the mass transfer.

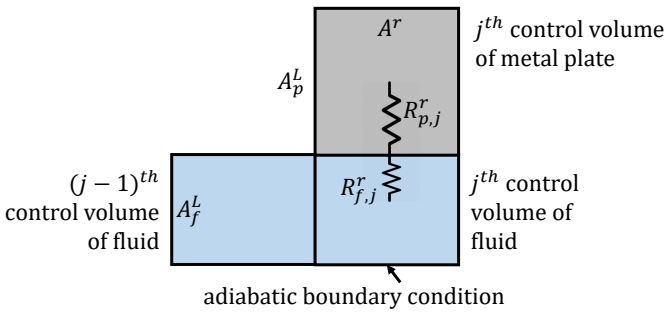

Figure 2.6. : Conductive and convective heat transfer between the fluid and the metal plate/tube control volumes.

$$\dot{Q}_j^f = \dot{Q}_j^{p\to f} + \dot{Q}_j^{flow} \implies m_f c_p^f \frac{dT_j^f}{dt} = \dot{Q}_j^{p\to f} + \dot{Q}_j^{flow} \tag{2.1}$$

Each term is expanded in Equation 2.2. The heat flux through the interface between the fluid and the metal plate/tube depends on the value of the convective heat transfer coefficient which is calculated using existing Nusselt number correlations for different types of flow regimes. For the first control volume of the fluid, T_{j-1}^f will be equal to T_{inlet}^f. For the last control volume of the fluid, T_{j+1}^f will be equal to T_j^f as there is no heat transfer process between the last control volume of the fluid in the fluid channel and the fluid outside the outlet of the fluid channel.

$$m_f c_p^f \frac{dT_j^f}{dt} = \frac{1}{R_{f,j}^r + R_{p-,j}^r}(T_j^p - T_j^f) + \dot{m}_f c_p^f (T_{j-1}^f - T_j^f) \tag{2.2}$$

The thermal resistance $R_{f,j}^r$ is a function of the convection coefficient $\alpha_{f,j}$ for the jth control volume of the fluid and the area of contact between the fluid control volume and the metal plate/tube control volume $A_{f,p}^r$. The length L_{char} in Equation 2.3 is the characteristic length of the fluid channel.

$$R_{f,j}^r = \frac{1}{\alpha_{f,j} A_{f,p}^r} \quad , \quad \alpha_{f,j} = Nu_j \frac{k_f}{L_{char}} \tag{2.3}$$

The thermal resistance $R^r_{p-,j}$, given by equation 2.4, is a function of the height of the metal plate/tube h_p, the conduction coefficient of the metal plate/tube k^r_p and the area of the surface parallel to the fluid-plate/tube interface A^r_{p-} at a distance $h_p/4$ from the fluid-plate/tube interface, defined away from the fluid flow axis.

$$R^r_{p-,j} = \frac{h_p}{2k^r_p A^r_{p-}} \tag{2.4}$$

The convective heat transfer coefficient is calculated using the Nusselt number, as shown in Equation 2.8, which in turn is calculated using existing Nusselt number correlations for different types of flow regimes [16]. The Nusselt number correlation for laminar flow is shown in Equation 2.5 where Nu_0 is equal to 5.39 for the extended plate geometry and is equal to 3.66 for the cylindrical tube geometry. The Nusselt number correlation for turbulent flow is shown in Equation 2.6. The friction factor f is used to calculate the Nusselt number for turbulent flow as shown in Equation 2.7 [17].

$$Nu = Nu_0 + \frac{0.0668\left(\frac{D}{L}\right) Re_D Pr}{1 + 0.04\left(\left(\frac{D}{L}\right) Re_D Pr\right)^{2/3}} \tag{2.5}$$

$$Nu = \frac{\left(\frac{f}{8}\right)(Re_D - 1000)\, Pr}{1 + 12.7\left(\frac{f}{8}\right)^{\frac{1}{2}}\left(\mathrm{Pr}^{\frac{2}{3}} - 1\right)} \tag{2.6}$$

$$f = 8\left(\left(\frac{8}{Re}\right)^{12} + \frac{1}{\left(\left(-2.2113\ln\left(\frac{7}{Re}\right)\right)^{16} + \left(\frac{37530}{Re}\right)^{16}\right)^{1.5}}\right)^{1/12} \tag{2.7}$$

$$\alpha_{f,j} = Nu_j \frac{k_f}{L_{char}} \tag{2.8}$$

Equation 2.9 describes the rate of change of energy contained within the metal plate/tube as shown in Figure 2.7, which is expanded as shown in Equation 2.10. The

rate of change of energy contained within the metal plate/tube is a function of the heat transferred from the fluid to the metal plate/tube and of the heat transferred from the metal plate/tube to the first sub-layer of the PCM.

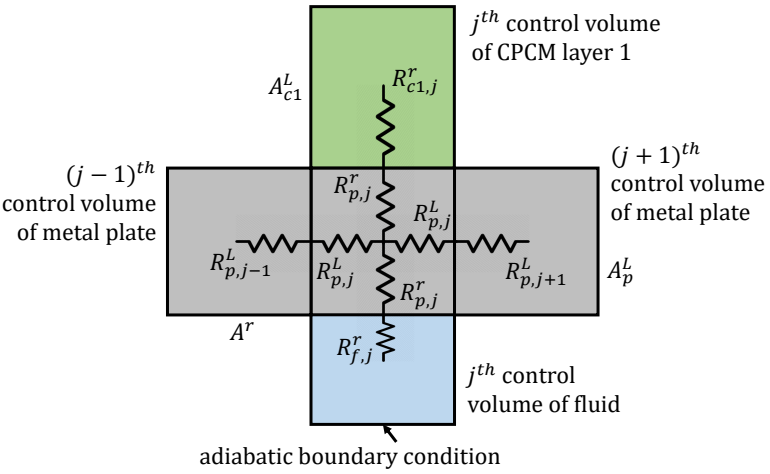

Figure 2.7. : Conductive and convective heat transfer between the metal plate/tube and the fluid and between the metal plate/tube and the CPCM sub-layer 1.

$$m_p c_p^p \frac{dT_j^p}{dt} = \dot{Q}_j^{f\to p} + \dot{Q}_j^{c1\to p} + \dot{Q}_{j-1\to j}^p + \dot{Q}_{j+1\to j}^p \tag{2.9}$$

$$m_p c_p^p \frac{dT_j^p}{dt} = \frac{1}{R^r_{f,j} + R^r_{p-,j}}(T_j^f - T_j^p) + \frac{1}{R^r_{p+,j} + R^r_{c1-,j}}(T_j^{c1} - T_j^p) + \frac{1}{R^L_{p,j-1} + R^L_{p,j}}(T_{j-1}^p - T_j^p) + \frac{1}{R^L_{p,j} + R^L_{p,j+1}}(T_{j+1}^p - T_j^p) \tag{2.10}$$

I assume adiabatic boundaries on the left and right side of the metal plate/tube. The thermal resistance $R^L_{p,j}$ is a function of the length of the jth control volume of the metal plate/tube l, the thermal conductivity of the jth control volume of the metal plate/tube k_p^L and the area of contact between the jth control volume of metal plate/tube and its neighbouring control volumes A_p^L. The thermal resistance $R^L_{p,j-1}$

for $j = 1$ and the thermal resistance $R^L_{p,j+1}$ for $j = n_L$, n_L being the total number of metal plate/tube control volumes, are taken to be infinitely large because there is no heat exchange through the outer boundaries of the two HX geometries.

$$R^L_{p,j} = \frac{l}{2k^L_p A^L_p} \tag{2.11}$$

The thermal resistance $R^r_{p+,j}$, shown in Equation 2.12, is a function of the height of the metal plate/tube h_p, the conduction coefficient of the metal plate/tube k^r_p and the area of the surface parallel to the fluid-plate/tube interface at a distance of $h_p/4$ from the center of the plate/tube A^r_{p+}, away from the fluid flow axis.

$$R^r_{p+,j} = \frac{h_p}{2k^r_p A^r_{p+}} \tag{2.12}$$

Similarly, $R^r_{c1-,j}$, shown in Equation 2.13 is a function of the height of the first CPCM sub-layer h_{c1}, the conduction coefficient of the CPCM sub-layer $k^r_{c1,j}$, and the area of the surface parallel to the fluid-plate/tube interface at a distance of $h_{c1}/4$ from the plate-CPCM layer interface A^r_{c1-}, away from the fluid flow axis.

$$R^r_{c1-,j} = \frac{h_{c1}}{2k^r_{c1,j} A^r_{c1-}} \tag{2.13}$$

To be consistent with the geometry and fin configuration depicted in Figure 2.2, the equivalent thermal conductivity for vertical and lateral heat transfer are calculated using Equations 2.14 and 2.15, respectively. Here, ϕ is the volume fraction of metal in the CPCM layer.

$$k^r_{ci} = \phi k_{metal} + (1 - \phi)k_{pcm} \tag{2.14}$$

$$k^L_{ci} = \frac{1}{\phi/k_{\text{metal}} + (1 - \phi)/k_{pcm}} \tag{2.15}$$

The rate of change of energy contained within the first sub-layer of the CPCM is given by Equation 2.16. Each term is expanded as shown in Equation 2.17. This is similar to Equation 2.10 in that it also assumes an adiabatic boundary condition on both the ends.

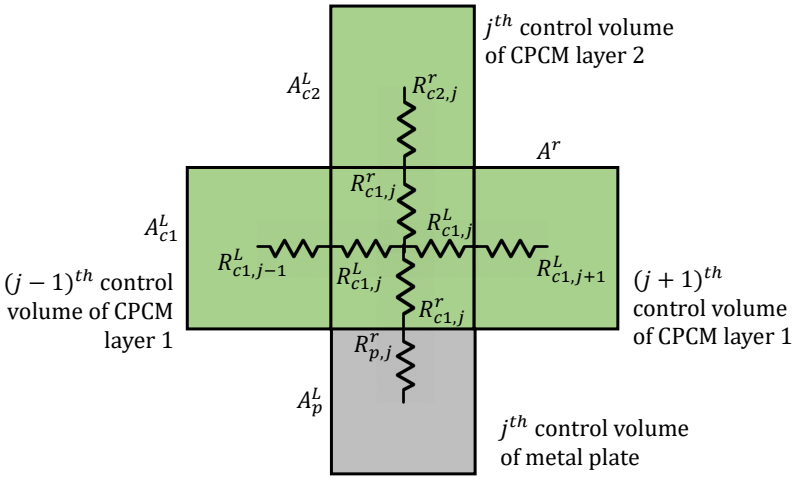

Figure 2.8. : Conductive heat transfer between metal plate/tube and the CPCM sub-layer 1 and between the CPCM sub-layer 1 and sub-layer 2.

$$m_{c1}c^{c1}_{p,j}\frac{dT^{c1}_j}{dt} = \dot{Q}^{p\to c1}_j + \dot{Q}^{c2\to c1}_j + \dot{Q}^{c1}_{j-1\to j} + \dot{Q}^{c1}_{j+1\to j} \tag{2.16}$$

$$\begin{aligned} m_{c1}c^{c1}_{p,j}\frac{dT^{c1}_j}{dt} = {} & \frac{1}{R^r_{p+,j}+R^r_{c1-,j}}(T^p_j - T^{c1}_j) + \frac{1}{R^r_{c1+,j}+R^r_{c2-,j}}(T^{c2}_j - T^{c1}_j) \\ & + \frac{1}{R^L_{c1,j-1}+R^L_{c1,j}}(T^{c1}_{j-1} - T^{c1}_j) + \frac{1}{R^L_{c1,j}+R^L_{c1,j+1}}(T^{c1}_{j+1} - T^{c1}_j) \end{aligned} \tag{2.17}$$

The thermal resistance $R^L_{c1,j}$, shown in Equation 2.18, is a function of the length of the jth control volume of the CPCM sub-layer 1 l, the thermal conductivity of the jth control volume of CPCM sub-layer 1 $k^L_{c1,j}$ and the area of contact between the jth control volume of CPCM sub-layer 1 and its neighbouring control volumes A^L_{c1}.

$$R^{L}_{c1,j} = \frac{l}{2k^{L}_{c1,j}A^{L}_{c1}} \tag{2.18}$$

The thermal resistance $R^{r}_{c1+,j}$, given by Equation 2.19, is a function of the height of the first CPCM sub-layer h_{c1}, the conduction coefficient of CPCM sub-layer $k^{r}_{c1,j}$ and the area of the surface parallel to the fluid-plate/tube interface at a distance of $h_{c1}/4$ from the center of CPCM sub-layer 1 A^{r}_{c1+}, away from the fluid flow axis.

$$R^{r}_{c1+,j} = \frac{h_{c1}}{2k^{r}_{c1,j}A^{r}_{c1+}} \tag{2.19}$$

Similarly, $R^{r}_{c2-,j}$, given by Equation 2.20, is a function of the height of CPCM sub-layer 2 h_{c2}, the conduction coefficient of CPCM sub-layer $k^{r}_{c2,j}$, and the area of the surface parallel to the fluid-plate/tube interface at a distance of $h_{c2}/4$ from the interface between CPCM sub-layers 1 and 2 A^{r}_{c2-}, away from the fluid flow axis.

$$R^{r}_{c2-,j} = \frac{h_{c2}}{2k^{r}_{c2,j}A^{r}_{c2-}} \tag{2.20}$$

Similarly, Equation 2.21 is expanded into Equation 2.22 and describes the rate of change of energy contained within the second sub-layer of the CPCM. This equation will be repeated $n_r - 2$ times, n_r being the total number of the CPCM sub-layers, and is a function of the heat transfer from two layers directly in contact with layer in consideration.

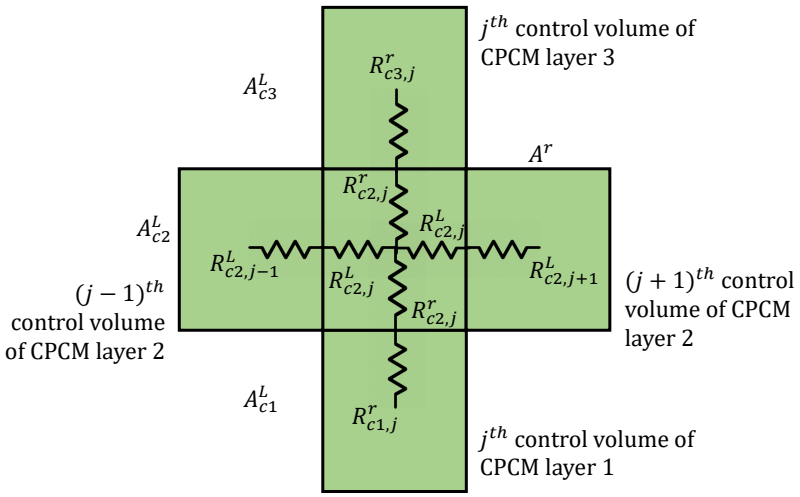

Figure 2.9. : Conductive heat transfer between CPCM sub-layer 1 and 2 and between CPCM sub-layer 2 and 3.

$$m_{c2}c^{c2}_{p,j}\frac{dT^{c2}_j}{dt} = \dot{Q}^{c1\to c2}_j + \dot{Q}^{c3\to c2}_j + \dot{Q}^{c2}_{j-1\to j} + \dot{Q}^{c2}_{j+1\to j} \tag{2.21}$$

$$\begin{aligned} m_{c2}c^{c2}_{p,j}\frac{dT^{c2}_j}{dt} = {} & \frac{1}{R^r_{c1+,j} + R^r_{c2-,j}}(T^{c1}_j - T^{c2}_j) + \frac{1}{R^r_{c2+,j} + R^r_{c3-,j}}(T^{c3}_j - T^{c2}_j) \\ & + \frac{1}{R^L_{c2,j-1} + R^L_{c2,j}}(T^{c2}_{j-1} - T^{c2}_j) + \frac{1}{R^L_{c2,j} + R^L_{c2,j+1}}(T^{c2}_{j+1} - T^{c2}_j) \end{aligned} \tag{2.22}$$

The thermal resistance $R^L_{c2,j}$, given by Equation 2.23, is a function of the length of the jth control volume of the CPCM sub-layer 2 l, the thermal conductivity of the jth control volume of CPCM sub-layer 2 $k^L_{c2,j}$ and the area of contact between the jth control volume of CPCM sub-layer 2 and its neighbouring control volumes A^L_{c2}.

$$R^L_{c2,j} = \frac{l}{2k^L_{c2,j}A^L_{c2}} \tag{2.23}$$

The thermal resistance $R^r_{c2+,j}$, given by Equation 2.24, is a function of the height of CPCM sub-layer 2 h_{c2}, the conduction coefficient of the CPCM sub-layer $k^r_{c2,j}$ and the area of the surface parallel to the fluid-plate/tube interface at a distance of $h_{c2}/4$ from the center of CPCM sub-layer 2 A^r_{c2+}, away from the fluid flow axis.

$$R^r_{c2+,j} = \frac{h_{c2}}{2k^r_{c2,j}A^r_{c2+}} \tag{2.24}$$

Similarly, $R^r_{c3-,j}$, given by Equation 2.25, is a function of the height of CPCM sub-layer 3 h_{c3}, the conduction coefficient of the CPCM sub-layer $k^r_{c3,j}$ and the area of the surface parallel to the fluid-plate/tube interface at a distance of $h_{c3}/4$ from the interface between CPCM sub-layers 2 and 3 A^r_{c3-}, away from the fluid flow axis.

$$R^r_{c3-,j} = \frac{h_{c3}}{2k^r_{c3,j}A^r_{c3-}} \tag{2.25}$$

The model equations for the 3rd to the $(n_L - 1)$th sub-layer of the CPCM will be similar to that of the 2nd sub-layer because the rate of change of the energy contained within any of these sub-layers will be a function of the heat transfer from the neighbouring sub-layers of the CPCM.

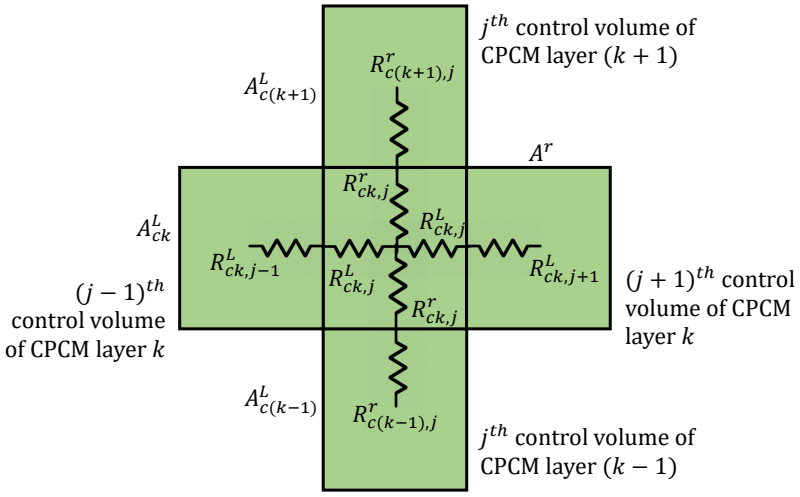

Figure 2.10. : Conductive heat transfer between the CPCM sub-layer *k-1* and layer k and between the CPCM sub-layer k and sub-layer *k+1*.

$$m_{ck}c^{ck}_{p,j}\frac{dT^{ck}_j}{dt} = \dot{Q}^{c(k-1)\to ck}_j + \dot{Q}^{c(k+1)\to ck}_j + \dot{Q}^{ck}_{j-1\to j} + \dot{Q}^{ck}_{j+1\to j} \tag{2.26}$$

$$\begin{aligned} m_{ck}c^{ck}_{p,j}\frac{dT^{ck}_j}{dt} = {} & \frac{1}{R^r_{c(k-1)+,j} + R^r_{ck-,j}}(T^{c(k-1)}_j - T^{ck}_j) + \frac{1}{R^r_{ck+,j} + R^r_{c(k+1)-,j}}(T^{c(k+1)}_j - T^{ck}_j) \\ & + \frac{1}{R^L_{ck,j-1} + R^L_{ck,j}}(T^{ck}_{j-1} - T^{ck}_j) + \frac{1}{R^L_{ck,j} + R^L_{ck,j+1}}(T^{ck}_{j+1} - T^{ck}_j) \end{aligned} \tag{2.27}$$

The thermal resistance $R^L_{ck,j}$, given by Equation 2.28, is a function of the length of the jth control volume of the CPCM sub-layer k, the thermal conductivity of the jth control volume of the CPCM sub-layer k ($k^L_{ck,j}$) and the area of contact between the jth control volume of the CPCM sub-layer k and its neighbouring control volumes A^L_{ck}.

$$R^L_{ck,j} = \frac{l}{2k^L_{ck,j}A^L_{ck}} \tag{2.28}$$

The thermal resistance $R^r_{ck+,j}$, given by Equation 2.29, is a function of the height of the CPCM sub-layer k (h_{ck}), the conduction coefficient of the CPCM sub-layer $k^r_{ck,j}$ and the area of the surface parallel to the fluid-plate/tube interface at a distance of $h_{ck}/4$ from the center of the CPCM sub-layer k (A^r_{ck+}), away from the fluid flow axis.

$$R^r_{ck+,j} = \frac{h_{ck}}{2k^r_{ck,j}A^r_{ck+}} \tag{2.29}$$

Similarly, $R^r_{c(k+1)-,j}$, given by Equation 2.30, is a function of the height of the CPCM sub-layer *k+1* ($h_{c(k+1)}$), the conduction coefficient of that CPCM sub-layer $k^r_{c(k+1),j}$ and the area of the surface parallel to the fluid-plate/tube interface at a distance of $h_{c(k+1)}/4$ from the interface between the CPCM sub-layers k and *k+1* ($A^r_{c(k+1)-}$), away from the fluid flow axis.

$$R^r_{c(k+1)-,j} = \frac{h_{c(k+1)}}{2k^r_{c(k+1),j}A^r_{c(k+1)-}} \tag{2.30}$$

Equation 2.31 describes the rate of change of energy contained within the n_rth sub-layer of the CPCM, which is expanded into Equation 2.32. It is a function of the heat transfer from the previous layer only as the boundary above the n_rth layer is assumed to be adiabatic.

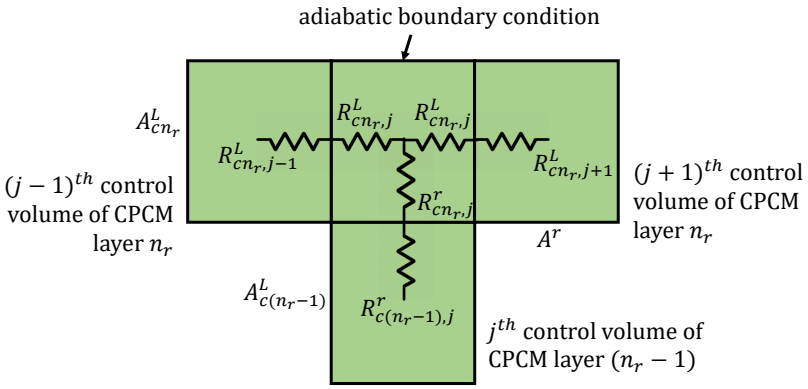

Figure 2.11. : Conductive heat transfer between the CPCM sub-layer n_r-1 and n_r.

$$m_{cn_r} c^{cn_r}_{p,j} \frac{dT^{cn_r}_j}{dt} = \dot{Q}^{c(n_r-1)\to cn_r}_j + \dot{Q}^{cn_r}_{j-1\to j} + \dot{Q}^{cn_r}_{j+1\to j} \tag{2.31}$$

$$\begin{aligned} m_{cn_r} c^{cn_r}_{p,j} \frac{dT^{cn_r}_j}{dt} &= \frac{1}{R^r_{c(n_r-1)+,j} + R^r_{cn_r-,j}} (T^{c(n_r-1)}_j - T^{cn_r}_j) \\ &+ \frac{1}{R^L_{cn_r,j-1} + R^L_{cn_r,j}} (T^{cn_r}_{j-1} - T^{cn_r}_j) + \frac{1}{R^L_{cn_r,j} + R^L_{cn_r,j+1}} (T^{cn_r}_{j+1} - T^{cn_r}_j) \end{aligned} \tag{2.32}$$

The thermal resistance $R^L_{cn_r,j}$, given by Equation 2.33, is a function of the length of the jth control volume of the CPCM sub-layer n_r, the thermal conductivity of the jth control volume of the CPCM sub-layer n_r ($k^L_{cn_r,j}$) and the area of contact between the jth control volume of the CPCM sub-layer n_r and its neighbouring control volumes $A^L_{cn_r}$.

$$R^L_{cn_r,j} = \frac{l}{2k^L_{cn_r,j} A^L_{cn_r}} \tag{2.33}$$

2.3.2 Matrix Formulation

Equations 2.2 through 2.33 are derived using the mass and energy balance equations for a j^{th} control volume of the fluid, the metal plate/tube and the CPCM layer. Now, I combine the equations for $j = 1, 2, 3..., n_L$, thus eliminating the subscript j used for tracking the control volume location in the horizontal direction. Equation 2.34 defines the mass matrix for the fluid, the plate/tube and the different sub-layers of the CPCM.

$$\mathbb{M}_i = \begin{bmatrix} m_i & 0 & 0 & \dots & 0 \\ 0 & m_i & 0 & \dots & 0 \\ 0 & 0 & m_i & \dots & 0 \\ \vdots & \vdots & \vdots & \ddots & \vdots \\ 0 & 0 & 0 & \dots & m_i \end{bmatrix}, \quad i = f, p, c1, c2, \dots, cn_r \tag{2.34}$$

Equation 2.35 defines the specific heat matrix for the fluid, the plate/tube and the different sub-layers of the CPCM.

$$\mathbb{C}_P^i = \begin{bmatrix} c_{p,1}^i & 0 & 0 & \dots & 0 \\ 0 & c_{p,2}^i & 0 & \dots & 0 \\ 0 & 0 & c_{p,3}^i & \dots & 0 \\ \vdots & \vdots & \vdots & \ddots & \vdots \\ 0 & 0 & 0 & \dots & c_{p,n_L}^i \end{bmatrix}, \quad i = f, p, c1, c2, \dots, cn_r \tag{2.35}$$

Equation 2.36 defines the temperature vector for the fluid, the plate/tube and the different sub-layers of the CPCM.

$$\mathbb{T}^i = \begin{bmatrix} T_1^i \\ T_2^i \\ T_3^i \\ \vdots \\ T_{n_L}^i \end{bmatrix}, \quad i = f, p, c1, c2, \ldots, cn_r \tag{2.36}$$

Equation 2.37 defines the matrix containing all the coefficients of the term $(T_j^p - T_j^f)$ in Equation 2.2 for $j = 1, 2, 3..., n_L$.

$$\mathbb{Z}_f^r = \begin{bmatrix} \frac{1}{R_{f,1}^r + R_{p-,1}^r} & 0 & 0 & \ldots & 0 \\ 0 & \frac{1}{R_{f,2}^r + R_{p-,2}^r} & 0 & \ldots & 0 \\ 0 & 0 & \frac{1}{R_{f,3}^r + R_{p-,3}^r} & \ldots & 0 \\ \vdots & \vdots & \vdots & \ddots & \vdots \\ 0 & 0 & 0 & \ldots & \frac{1}{R_{f,n_L}^r + R_{p-,n_L}^r} \end{bmatrix} \tag{2.37}$$

Equation 2.38 defines the matrix containing all the coefficients of the term $(T_j^{c1} - T_j^p)$ in Equation 2.10 for $j = 1, 2, 3..., n_L$.

$$\mathbb{Z}_p^r = \begin{bmatrix} \frac{1}{R_{p+,1}^r + R_{c1-,1}^r} & 0 & 0 & \ldots & 0 & \\ 0 & \frac{1}{R_{p+,2}^r + R_{c1-,2}^r} & 0 & \ldots & 0 & \\ 0 & 0 & \frac{1}{R_{p+,3}^r + R_{c1-,3}^r} & \ldots & 0 & \\ \vdots & \vdots & \vdots & \vdots & \ddots & \vdots \\ 0 & 0 & 0 & \ldots & \frac{1}{R_{p+,n_L}^r + R_{c1-,n_L}^r} & \end{bmatrix} \tag{2.38}$$

Equation 2.39 defines the matrix containing the coefficients of the term $(T_{j-1}^p - T_j^p)$ in Equation 2.10 for $j = 1, 2, 3..., n_L$.

$$\mathbb{Z}^L_{p-} = \begin{bmatrix} \frac{1}{R^L_{p,0}+R^L_{p,1}} & 0 & 0 & \dots & 0 \\ 0 & \frac{1}{R^L_{p,1}+R^L_{p,2}} & 0 & \dots & 0 \\ 0 & 0 & \frac{1}{R^L_{p,2}+R^L_{p,3}} & \dots & 0 \\ \vdots & \vdots & \vdots & \ddots & \vdots \\ 0 & 0 & 0 & \dots & \frac{1}{R^L_{p,n_L-1}+R^L_{p,n_L}} \end{bmatrix} \tag{2.39}$$

Equation 2.40 defines the matrix containing all the coefficients of the term $(T^p_{j+1} - T^p_j)$ in Equation 2.10 for $j = 1, 2, 3..., n_L$.

$$\mathbb{Z}^L_{p+} = \begin{bmatrix} \frac{1}{R^L_{p,1}+R^L_{p,2}} & 0 & 0 & \dots & 0 \\ 0 & \frac{1}{R^L_{p,2}+R^L_{p,3}} & 0 & \dots & 0 \\ 0 & 0 & \frac{1}{R^L_{p,3}+R^L_{p,4}} & \dots & 0 \\ \vdots & \vdots & \vdots & \ddots & \vdots \\ 0 & 0 & 0 & \dots & \frac{1}{R^L_{p,n_L}+R^L_{p,n_L+1}} \end{bmatrix} \tag{2.40}$$

Equation 2.41 defines the matrix containing all the coefficients of the term $(T^{c2}_j - T^{c1}_j)$ in Equation 2.17 for $j = 1, 2, 3..., n_L$.

$$\mathbb{Z}^r_{c1} = \begin{bmatrix} \frac{1}{R^r_{c1+,1}+R^r_{c2-,1}} & 0 & 0 & \dots & 0 \\ 0 & \frac{1}{R^r_{c1+,2}+R^r_{c2-,2}} & 0 & \dots & 0 \\ 0 & 0 & \frac{1}{R^r_{c1+,3}+R^r_{c2-,3}} & \dots & 0 \\ \vdots & \vdots & \vdots & \ddots & \vdots \\ 0 & 0 & 0 & \dots & \frac{1}{R^r_{c1+,n_L}+R^r_{c2-,n_L}} \end{bmatrix} \tag{2.41}$$

Equation 2.42 defines the matrix containing all the coefficients of the term $(T^{c1}_{j-1} - T^{c1}_j)$ in Equation 2.17 for $j = 1, 2, 3..., n_L$.

$$\mathbb{Z}^L_{c1-} = \begin{bmatrix} \frac{1}{R^L_{c1,0}+R^L_{c1,1}} & 0 & 0 & \dots & 0 \\ 0 & \frac{1}{R^L_{c1,1}+R^L_{c1,2}} & 0 & \dots & 0 \\ 0 & 0 & \frac{1}{R^L_{c1,2}+R^L_{c1,3}} & \dots & 0 \\ \vdots & \vdots & \vdots & \ddots & \vdots \\ 0 & 0 & 0 & \dots & \frac{1}{R^L_{c1,n_L-1}+R^L_{c1,n_L}} \end{bmatrix} \tag{2.42}$$

Equation 2.43 defines the matrix containing all the coefficients of the term $(T^{c1}_{j+1} - T^{c1}_{j})$ in Equation 2.10 for $j = 1, 2, 3..., n_L$.

$$\mathbb{Z}^L_{c1+} = \begin{bmatrix} \frac{1}{R^L_{c1,1}+R^L_{c1,2}} & 0 & 0 & \dots & 0 \\ 0 & \frac{1}{R^L_{c1,2}+R^L_{c1,3}} & 0 & \dots & 0 \\ 0 & 0 & \frac{1}{R^L_{c1,3}+R^L_{c1,4}} & \dots & 0 \\ \vdots & \vdots & \vdots & \ddots & \vdots \\ 0 & 0 & 0 & \dots & \frac{1}{R^L_{c1,n_L}+R^L_{c1,n_L+1}} \end{bmatrix} \tag{2.43}$$

Similarly, matrices $\mathbb{Z}^r_{c2}$, $\mathbb{Z}^L_{c2-}$, $\mathbb{Z}^L_{c2+}$ and so on can be defined for all the sub-layers of the CPCM.

The matrices defined using Equations 2.34 through 2.43 are contained in $\Re^{n_L \times n_L}$. Using matrices $\mathbb{D}_-$, $\mathbb{D}_+$ and $\mathbb{D}$ defined in Equation 2.44, the rate of change of the energy contained within the working fluid is given by Equation 2.45. The matrix I is an identity matrix of size $n_L \times n_L$.

$$\mathbb{D}_- = \begin{bmatrix} 0 & 0 & \dots & 0 & 0 \\ 1 & 0 & \dots & 0 & 0 \\ 0 & 1 & \dots & 0 & 0 \\ \vdots & \vdots & \ddots & \vdots & \vdots \\ 0 & 0 & \dots & 1 & 0 \end{bmatrix}, \mathbb{D}_+ = \begin{bmatrix} 0 & 1 & 0 & \dots & 0 \\ 0 & 0 & 1 & \dots & 0 \\ \vdots & \vdots & \vdots & \ddots & \vdots \\ 0 & 0 & 0 & \dots & 1 \\ 0 & 0 & 0 & \dots & 0 \end{bmatrix}, \mathbb{D} = \begin{bmatrix} 1 & 0 & 0 & \dots & 0 \\ 0 & 0 & 0 & \dots & 0 \\ 0 & 0 & 0 & \dots & 0 \\ \vdots & \vdots & \vdots & \ddots & \vdots \\ 0 & 0 & 0 & \dots & 0 \end{bmatrix} \quad (2.44)$$

$$\mathbb{M}_f \mathbb{C}_P^f \frac{d\mathbb{T}^f}{dt} = \mathbb{Z}_f^r T^p + \Big(- \mathbb{Z}_f^r + \dot{\mathbb{M}}_f \mathbb{C}_P^f (\mathbb{D}_- - I) \Big) \mathbb{T}^f + \dot{\mathbb{M}}_f \mathbb{C}_P^f \mathbb{D} \mathbb{T}_{in}^f \quad (2.45)$$

Equation 2.46 describes the rate of change of heat energy contained within the metal plate/tube, which includes all the control volumes of metal plate/tube.

$$\mathbb{M}_p \mathbb{C}_P^p \frac{d\mathbb{T}^p}{dt} = \mathbb{Z}_f^r \mathbb{T}^f + \Big(- \mathbb{Z}_f^r + \mathbb{Z}_p^L (\mathbb{D}_- + \mathbb{D}_+ - 2I) - \mathbb{Z}_p^r \Big) \mathbb{T}^p + \mathbb{Z}_p^r \mathbb{T}^{c1} \quad (2.46)$$

Equation 2.47 describes the rate of change of heat energy contained within the 1st sub-layer of the CPCM, which includes all the control volumes of that layer.

$$\mathbb{M}_{c1} \mathbb{C}_P^{c1} \frac{d\mathbb{T}^{c1}}{dt} = \mathbb{Z}_p^r \mathbb{T}^p + \Big(- \mathbb{Z}_p^r + \mathbb{Z}_{c1}^L (\mathbb{D}_- + \mathbb{D}_+ - 2I) - \mathbb{Z}_{c1}^r \Big) \mathbb{T}^{c1} + \mathbb{Z}_{c1}^r \mathbb{T}^{c2} \quad (2.47)$$

Equation 2.48 describes the rate of change of heat energy contained within the 2nd sub-layer of the CPCM, which includes all the control volumes of that layer.

$$\mathbb{M}_{c2}\mathbb{C}_P^{c2}\frac{d\mathbb{T}^{c2}}{dt} = \mathbb{Z}_{c1}^r\mathbb{T}^{c1} + \Big(- \mathbb{Z}_{c1}^r + \mathbb{Z}_{c2}^L(\mathbb{D}_- + \mathbb{D}_+ - 2I) - \mathbb{Z}_{c2}^r\Big)\mathbb{T}^{c2} + \mathbb{Z}_{c2}^r\mathbb{T}^{c3} \quad (2.48)$$

Equation describing the rate of change of heat energy contained within the 3rd to the $n_r - 1$ sub-layer of the CPCM will be similar to Equation 2.48. Equation 2.49 describes the rate of change of heat energy contained within the n_r sub-layer of the CPCM, which includes all the control volumes of that layer.

$$\mathbb{M}_{cn_r}\mathbb{C}_P^{cn_r}\frac{d\mathbb{T}^{cn_r}}{dt} = \mathbb{Z}_{c(n_r-1)}^r\mathbb{T}^{c(n_r-1)} + \Big(- \mathbb{Z}_{c(n_r-1)}^r + \mathbb{Z}_{cn_r}^L(\mathbb{D}_- + \mathbb{D}_+ - 2I)\Big)\mathbb{T}^{cn_r} \quad (2.49)$$

2.3.3 Overall System Formulation

Equations 2.45 through 2.49 can further be combined to form a single ordinary differential equation (ODE) as shown in Equation 2.50. The first order differentiation of a variable x with respect to time is written as $\dot{x}$.

$$\mathbb{A}_O\dot{\mathbb{T}}_O = \mathbb{B}_O\mathbb{T}_O + \mathbb{C}_O \quad (2.50)$$

The matrix $\mathbb{A}_O \in \Re^{(2+n_r)n_L \times (2+n_r)n_L}$, shown in Equation 2.51, is the overall system matrix with all the diagonal entries as the product of the mass matrices and the specific heat matrices defined in Subsection 2.3.2.

$$\mathbb{A}_O = \begin{bmatrix} \mathbb{M}_f\mathbb{C}_P^f & 0 & 0 & \dots & 0 \\ 0 & \mathbb{M}_p\mathbb{C}_P^p & 0 & \dots & 0 \\ 0 & 0 & \mathbb{M}_{c1}\mathbb{C}_P^{c1} & \dots & 0 \\ \vdots & \vdots & \vdots & \ddots & \vdots \\ 0 & 0 & 0 & \dots & \mathbb{M}_{cn_r}\mathbb{C}_P^{cn_r} \end{bmatrix} \tag{2.51}$$

The matrix $\mathbb{B}_O \in \Re^{(2+n_r)n_L \times (2+n_r)n_L}$, shown in Equation 2.52, is the overall system matrix with different entries as the coefficients of the temperature vector of the fluid, the metal plate/tube and the different CPCM sub-layers. Each term is expanded and tabulated in Table 2.1.

$$\mathbb{B}_O = \begin{bmatrix} \mathbb{B}_{1,1} & \mathbb{B}_{1,2} & 0 & \dots & 0 \\ \mathbb{B}_{2,1} & \mathbb{B}_{2,2} & \mathbb{B}_{2,3} & \dots & 0 \\ 0 & \mathbb{B}_{3,2} & \mathbb{B}_{3,3} & \dots & 0 \\ \vdots & \vdots & \vdots & \ddots & \vdots \\ 0 & 0 & 0 & \dots & \mathbb{B}_{n_r+2,n_r+2} \end{bmatrix} \tag{2.52}$$

The matrix $\mathbb{C}_O \in \Re^{(2+n_r)n_L \times (2+n_r)n_L}$ is defined in Equation 2.53. The inlet temperature of the fluid is defined as T_{in}^f.

$$\mathbb{C}_O = \begin{bmatrix} \dot{\mathbb{M}}^f\mathbb{C}_P^f\mathbb{D}_0 & 0 & 0 & \dots & 0 \\ 0 & 0 & 0 & \dots & 0 \\ 0 & 0 & 0 & \dots & 0 \\ \vdots & \vdots & \vdots & \ddots & \vdots \\ 0 & 0 & 0 & \dots & 0 \end{bmatrix} T_{in}^f \tag{2.53}$$

The vector $\mathbb{T}_O \in \Re^{(2+n_r)n_L}$ is a vector containing the temperature variables of all the controls volumes of the system. It is shown in Equation 2.54.

Table 2.1. : Values of entries of the matrix $\mathbb{B}_O$

Entry	**Value**
$\mathbb{B}_{1,1}$	$\mathbb{Z}_f^L(\mathbb{D}_- + \mathbb{D}_+ - 2I) - \mathbb{Z}_f^r + \dot{\mathbb{M}}_f\mathbb{C}_P^f(\mathbb{D}_- - I)$
$\mathbb{B}_{1,2}$	$\mathbb{Z}_f^r$
$\mathbb{B}_{2,1}$	$\mathbb{Z}_f^r$
$\mathbb{B}_{2,2}$	$-\mathbb{Z}_f^r + \mathbb{Z}_p^L(\mathbb{D}_- + \mathbb{D}_+ - 2I) - \mathbb{Z}_p^r$
$\mathbb{B}_{2,3}$	$\mathbb{Z}_p^r$
$\mathbb{B}_{3,2}$	$\mathbb{Z}_p^r$
$\mathbb{B}_{3,3}$	$-\mathbb{Z}_p^r + \mathbb{Z}_{c1}^L(\mathbb{D}_- + \mathbb{D}_+ - 2I) - \mathbb{Z}_{c1}^r$
$\mathbb{B}_{3,4}$	$\mathbb{Z}_{c1}^r$
$\mathbb{B}_{4,3}$	$\mathbb{Z}_{c1}^r$
$\mathbb{B}_{4,4}$	$-\mathbb{Z}_{c1}^r + \mathbb{Z}_{c2}^L(\mathbb{D}_- + \mathbb{D}_+ - 2I) - \mathbb{Z}_{c2}^r$
$\vdots$	$\vdots$
$\mathbb{B}_{n_r+1,n_r+2}$	$\mathbb{Z}_{c(n_r-1)}^r$
$\mathbb{B}_{n_r+2,n_r+1}$	$\mathbb{Z}_{c(n_r-1)}^r$
$\mathbb{B}_{n_r+2,n_r+2}$	$-\mathbb{Z}_{c(n_r-1)}^r + \mathbb{Z}_{cn_r}^L(\mathbb{D}_- + \mathbb{D}_+ - 2I)$

$$\mathbb{T}_O = \begin{bmatrix} \mathbb{T}^f & \mathbb{T}^p & \mathbb{T}^{c1} & \dots & \mathbb{T}^{cn_r} \end{bmatrix}^T \tag{2.54}$$

2.4 Numerical Solution

The model is coded and simulated in the Python programming environment. To solve the model equations, I use the backward Euler method (an implicit solution method) to discretize the ODE shown in 2.50. Using a time-step of Δt, I derive the approximate model in Equation 2.55. The temperature $\mathbb{T}_O(p)$ represents the temperature value at the pth iteration.

$$\mathbb{A}_O \frac{\mathbb{T}_O(p) - \mathbb{T}_O(p-1)}{\Delta t} = \mathbb{B}_O \mathbb{T}_O(p) + \mathbb{C}_O \tag{2.55}$$

Rearranging Equation 2.55, such that the temperature at a current iteration p is a function of the temperature at the previous iteration $p-1$, gives Equation 2.56 which can be solved in an iterative manner for a known initial condition.

$$\mathbb{T}_O(p) = (\mathbb{A}_O - \Delta t \mathbb{B}_O)^{-1} (\mathbb{A}_O \mathbb{T}_O(p-1) + \Delta t \mathbb{C}_O) \tag{2.56}$$

Furthermore, to simulate the melting of PCM, we use the algorithm shown in Figure 2.12. Here, E is the net energy transferred into a control volume of composite PCM during an iteration, E_{melt} is the energy required to completely melt a control volume of composite PCM, p is the current iteration, i_{final} is the total number of iterations, and m is the melt fraction of a control volume of the CPCM at any given time. Once a CPCM control volume starts melting, the properties of that control volume are calculated by taking a weighted average of solid PCM properties and liquid PCM properties using the melt fraction of that control volume. Properties are

updated after every iteration based on the extent of melting or solidification that has occurred.

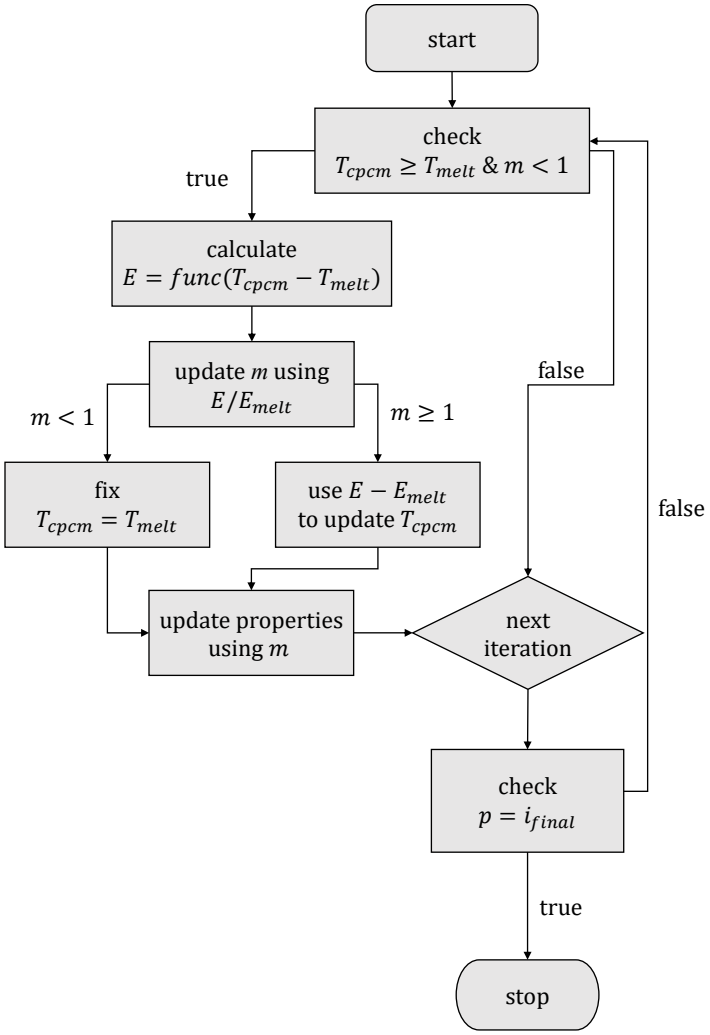

Figure 2.12. : Flow chart describing the algorithm for the melting of each composite PCM layer control volume in the reduced-order model.

3. MODEL VALIDATION

In this chapter, I compare the predictions of the reduced-order model against those of a high fidelity CFD model of the same geometry developed in the modeling package ANSYS Fluent. I first describe the ANSYS Fluent model and then present and discuss comparative plots between that and the proposed reduced-order model. The CFD model was developed by Michael Deckard at Texas A&M University.

3.1 ANSYS Fluent Model

Detailed simulations of melting within the extended flat plate heat exchanger and the cylindrical tube heat exchanger are completed within ANSYS Fluent, following these six steps: 1) system definition, 2) mesh generation, 3) definition of boundary and initial conditions, 4) definition of relevant physics, 5) setting of the solver conditions, and 6) execution of the model simulation. The simulated geometries used were described in Section 2.1. Within ANSYS, the extended flat plate geometry is represented as a 2D geometry with a mirror symmetry boundary to reduce the simulation complexity. The cylindrical geometry is treated as a 2D geometry that is assumed to have radial symmetry, instead of a mirror symmetry boundary. All non-fluid flow (outside) boundaries (top, bottom, left, right) are treated as adiabatic boundaries. Material properties for all materials in the simulation are given in Table 3.1.

Table 3.1. : Material properties of the fluid, the metal and the PCM used to simulate the CFD models of the two HXs in ANSYS Fluent.

	Metal (Al)	Solid PCM ($LiNO_3 \cdot 3H_2O$)	Liquid PCM ($LiNO_3 \cdot 3H_2O$)	Fluid (H_2O)
Density, kg/m^3	2719	1575	1425	998.2
Specific heat capacity, J/kg·K	871	1730	2760	4182
Thermal conductivity coefficient, W/m·K	202.4	0.82	0.584	0.6
Latent heat of fusion, J/kg	-	287000	287000	-
Viscosity, μPa·s	-	-	17.2	79.8
Melting temperature, K	-	303.3	303.3	-

3.1.1 Mesh Generation

The mesh created in ANSYS is generated automatically by following mesh setup specifications. The fluid channel is meshed to a finer size than the remainder of the simulation geometry due to the fidelity required in Fluent for accurately simulating the fluid flow. The element sizing used is 0.0379 mm square grid spacing for the channel, and 0.165 mm square grid spacing for the remaining regions. A close-up of the resulting mesh is shown in Figure 3.1.

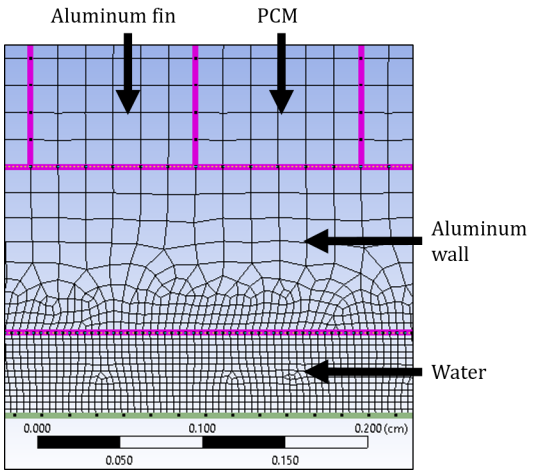

Figure 3.1. : Close-up view of mesh in ANSYS Fluent.

3.1.2 Boundary and Initial Conditions

A velocity boundary condition was applied to the inlet of each geometry with a specified flow rate and a temperature corresponding to the desired simulation. In order to minimize the length of the channel through which the velocity profile "developed", a brief simulation was run, and the resulting velocity profile at the outlet was used as the new velocity profile at the inlet. This process was repeated until the velocity profile no longer changed, and the resulting velocity profile was chosen as the velocity profile for the inlet boundary condition. This process was used for both the laminar and turbulent cases. A pressure outlet condition of zero gauge pressure was set at the outlet of the fluid channel for each geometry.

Heat transfer across the solid/liquid interfaces (e.g., aluminum-water interface) within ANSYS results from the coupled solution of the conductive heat transfer equations for the solid state and the Navier-Stokes equations for the adjacent fluid domain. Thus, the temperature and the heat transfer coefficients at the fluid-solid interface are determined by a local energy balance, rather than deriving from an empirical heat transfer correlation. The contact thermal resistance values at any of the interfaces

are set to be zero. After the initialization of the simulation, the initial temperature was set to 303.3 K uniformly throughout the entire simulated volume so as to be equal to the PCM melting temperature. This restricts the simulations to be single-phase, which simplifies simulation and interpretation. In addition, at the beginning of each simulation, the fluid channel does not contain hot fluid which allows for a more realistic simulation of hot fluid entering the fluid channel as the simulation starts.

3.1.3 Problem Physics

Depending on the simulation, either the laminar or Spalart-Allmaras viscous models were used to simulate the fluid flow [18]. The energy model was included, as well as solidification and melting physics. The energy model activated equations and calculations for heat transfer within ANSYS. The solidification and melting physics in the model utilizes the enthalpy method with a single melting point [19]. This suppresses temperature changes in a given element while the element changes phase. The PCM has temperature-dependent density, and a discontinuity in density between the solid and the liquid phases. Gravity is disabled and thus no buoyancy-driven convection is present in either the liquid PCM volumes, or in the fluid channel. The excess PCM volume within the simulated space is removed by ANSYS during expansion, but this amount is negligible in comparison to the total PCM volume for both geometries.

3.1.4 Solver Conditions

The default values are used for under-relaxation, including 0.9 for liquid fraction update and 1 for energy under-relaxation. The scheme of Pressure-Implicit with Splitting of Operators is used for pressure-velocity coupling, and second order discretization is used for pressure, momentum, turbulent viscosity (when appropriate),

energy and transient formulation. Fixed time steps of 1 s were used for both geometries for the laminar condition, and fixed time steps of 0.01 s were used for both geometries for the turbulent condition.

3.2 Validation Results

Here I present a temporal and spatial validation of the two heat exchanger geometries with the integrated PCM for both laminar and turbulent flow. These results reflect the combined effect of all the modeling assumptions made in deriving the reduced-order model. The material properties of fluid, metal and PCM are tabulated in Table 3.2. In the validation results that follow, the ANSYS Fluent model is referred to as the high fidelity (HF) model, and the reduced-order model is referred to as the low fidelity (LF) model. The low fidelity model prediction at the ith spatial validation location is referred as 'LF i' and the high fidelity model prediction at the same location is referred as 'HF i', for i ranging from 1 to 10. Note that validation results for i=2,4,6,8 are omitted to improve the readability of Figures 3.2 through 3.17.

Table 3.2. : Material properties of the fluid, the metal and the PCM used to simulated the reduced-order models of the two HXs.

	Metal (Al)	Solid PCM ($LiNO_3 \cdot 3H_2O$)	Liquid PCM ($LiNO_3 \cdot 3H_2O$)	Fluid (H_2O)
Density, kg/m^3	2719	1500	1500	998.2
Specific heat capacity, J/kg·K	871	1730	2760	4182
Thermal conductivity coefficient, W/m·K	202.4	0.82	0.584	0.6
Latent heat of fusion, J/kg	-	287000	287000	-
Viscosity, μPa·s	-	-	-	-
Melting temperature, K	-	303.3	303.3	-

3.2.1 Extended Flat Plate Geometry

First I consider the laminar fluid flow results for the extended flat plate geometry and then I move to the turbulent fluid flow case. The height of the fluid channel, the height of the metal plate, the height of the CPCM layer and the length of the HX for laminar and turbulent cases are 0.5 mm, 1 mm, 1 cm and 10 cm, respectively.

Laminar Flow

In the case of laminar flow, the reduced-order model as well as the CFD ANSYS Fluent model were simulated for 200 seconds with a fluid velocity of 0.1 m/s. The number of fluid control volumes n_L considered in the reduced-order model was 70, and the number of CPCM sub-layers n_r considered was 50.

Figure 3.2 shows a comparison of the fluid temperature predicted by each model, both spatially and temporally. The transient fluid temperature trajectories predicted by the LF model generally match those predicted by the HF model, with a normalized root mean square error (NRMSE) of 1.9% in the magnitude of the average fluid temperature, shown by Figure 3.2(b), between the two models. All NRMSE values listed in this chapter are calculated based upon averaged signals for the temperature, the melt fraction or the heat flux evolution for different geometries with laminar and turbulent fluid flow. More specifically, the ten time-varying signals for each variable of interest (representing different locations along the length of the fluid channel in each geometry) are averaged, and then the NRMSE is calculated based upon this averaged signal. The NRMSE is calculated using Equation 3.1, where $\hat{Z}_i$ is the estimated variable and Z_i is the true variable, and S is the sample size.

$$NRMSE = \frac{\sum_{i=1}^{S} \sqrt{\left(\hat{Z}_i - Z_i\right)^2 / S}}{Z_{i,max} - Z_{i,min}} \tag{3.1}$$

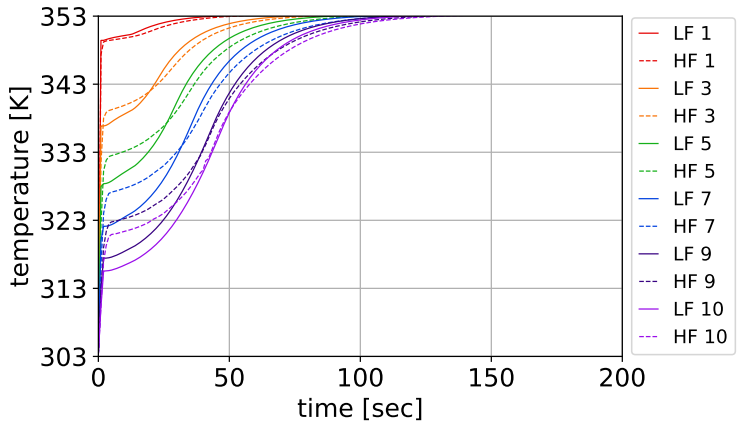

(a) The fluid temperature at different locations plotted as a function of time.

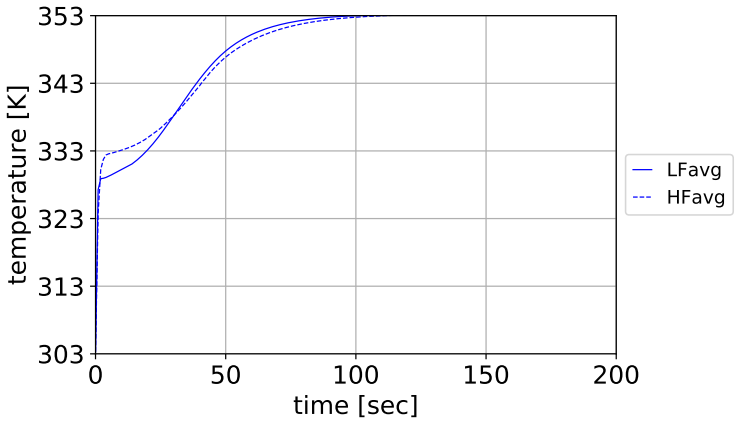

(b) The average fluid temperature plotted as a function of time.

Figure 3.2. : Temporal and spatial comparison of the fluid temperature for laminar flow in the extended flat plate geometry.

Figure 3.3 and Figure 3.4 compare the metal plate temperature and melt fraction of PCM, respectively, as predicted by each model. The NRMSE in the magnitude of the metal plate temperature as predicted by each model is 3.5%. Furthermore, there is a NRMSE of 2.8% in the magnitude of the melt fraction across the CPCM layer.

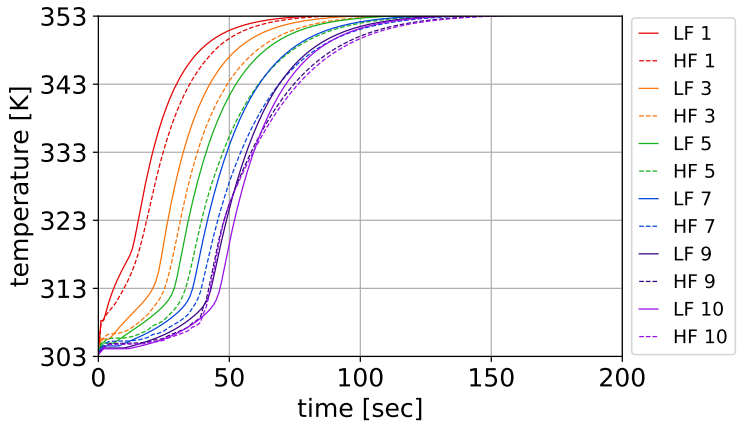

(a) The metal plate temperature at different locations plotted as a function of time.

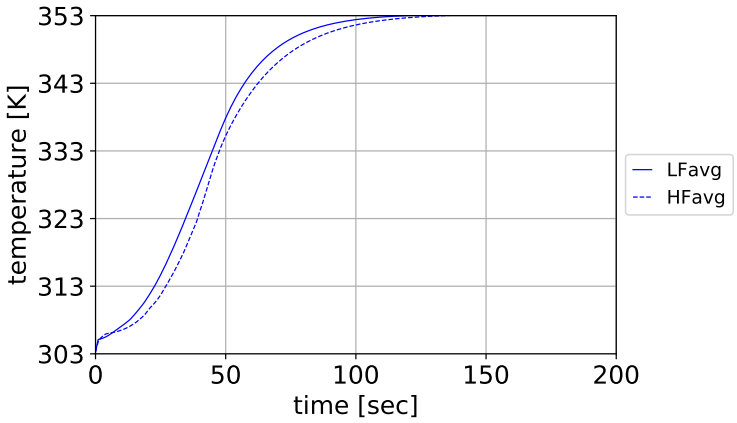

(b) The average metal plate temperature plotted as a function of time.

Figure 3.3. : Temporal and spatial comparison of the metal plate temperature for laminar flow in the extended flat plate geometry.

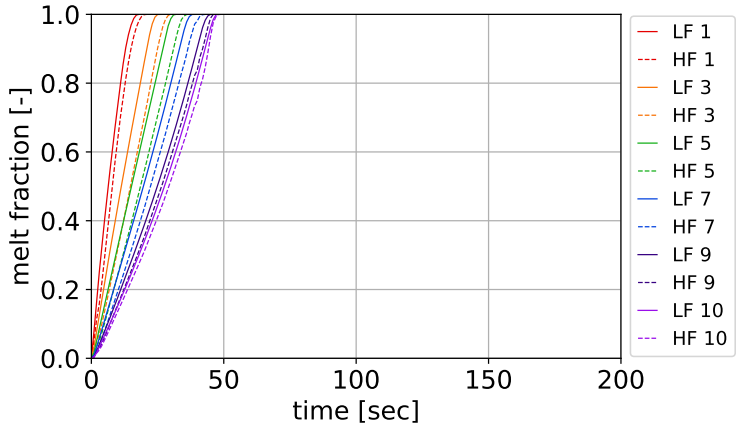

(a) The melt fraction of PCM at different locations plotted as a function of time.

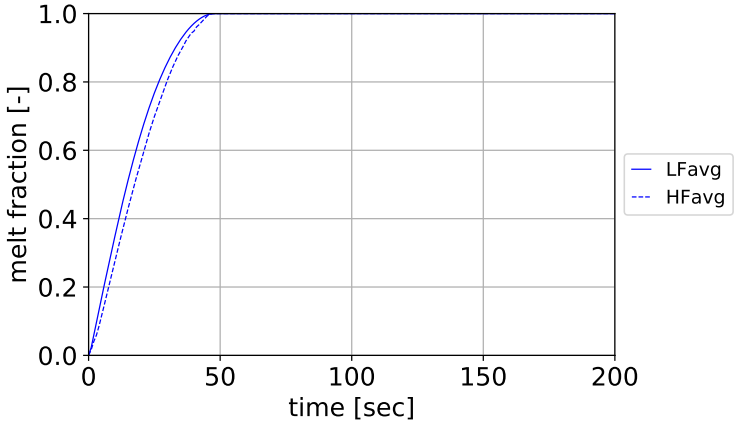

(b) The average melt fraction of PCM plotted as a function of time.

Figure 3.4. : Temporal and spatial comparison of the melt fraction of PCM for laminar flow in the extended flat plate geometry.

Finally, there is a NRMSE of 7% in the magnitude of heat flux, through the fluid-metal plate interface, between the two models. The heat flux across the fluid-metal plate interface predicted by the LF model is initially higher than that predicted by the HF model, as shown in Figure 3.5. This is consistent with the fluid temperature comparison shown in Figure 3.2, where the initial temperature of fluid as predicted by the LF model is lower than that predicted by the HF model, and with the melt fraction comparison shown in Figure 3.4, where the melt fraction of PCM as predicted by the

LF model is higher than that predicted by the HF model. I attribute the discrepancy to the lumped parameter assumption applied to the LF model which precludes the model from considering viscosity gradients within individual control volumes. This assumption may be less accurate when large temperature differences exist between the fluid and the metal plate. A viscosity gradient would affect the velocity profile, which in turn affects the temperature profile and heat transfer rate. Nevertheless, these results demonstrate good agreement temporally and spatially between the two models for the laminar flow case.

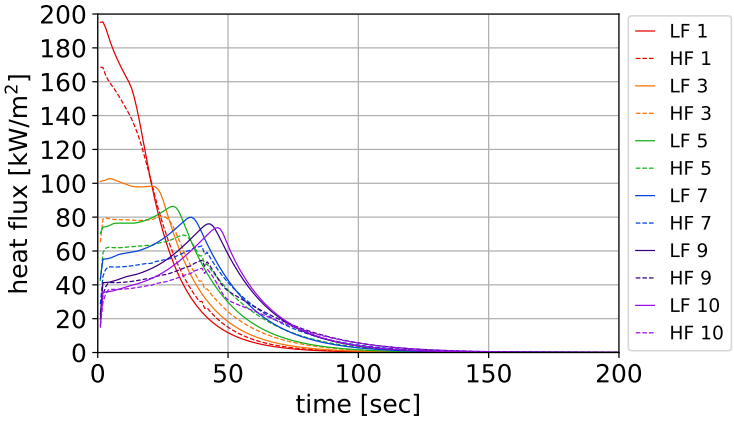

(a) The heat flux through the fluid-metal plate interface at different locations plotted as a function of time.

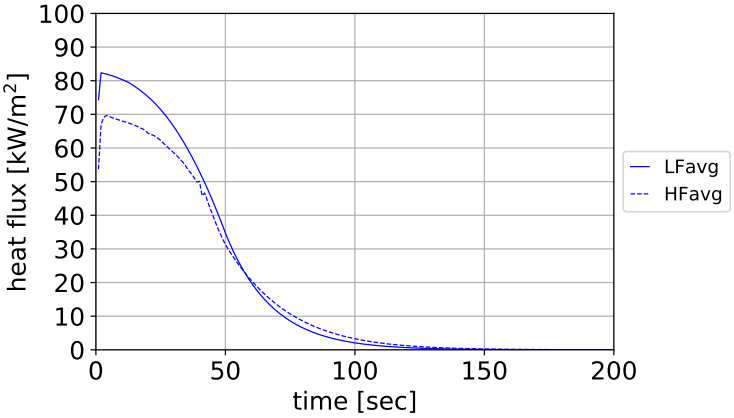

(b) The average heat flux through the fluid-metal plate interface plotted as a function of time.

Figure 3.5. : Temporal and spatial comparison of the heat flux through the fluid-metal plate interface for laminar flow in the extended flat plate geometry.

Turbulent Flow

In the case of turbulent flow, both models were simulated for 20 seconds and a fluid velocity of 4 meters per second. The number of fluid control volumes n_L considered in the LF model was 70, and the number of PCM layers n_r considered was 50.

Figure 3.6 compares the fluid temperature predicted by each model. The NRMSE across the length of the fluid channel was calculated to be 0.4%.

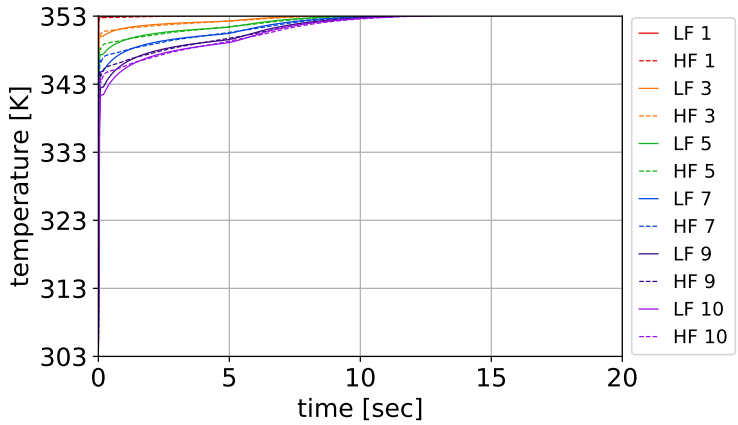

(a) The fluid temperature at different locations plotted as a function of time.

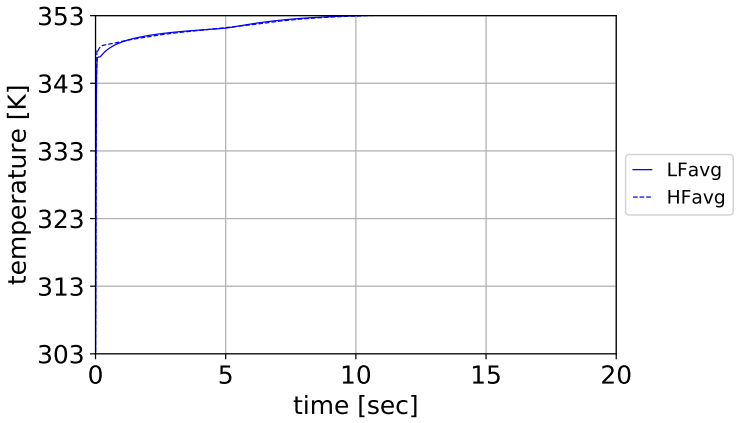

(b) The average fluid temperature plotted as a function of time.

Figure 3.6. : Temporal and spatial comparison of the fluid temperature for turbulent flow in the extended flat plate geometry.

Figure 3.7 compares the temperature of the metal plate as predicted by each model, where the NRMSE is 2.4%. Figure 3.8 compares the melt fraction of PCM within the CPCM layer as predicted by each model. The NRMSE in the magnitude of the melt fraction across the CPCM layer is 6.4%.

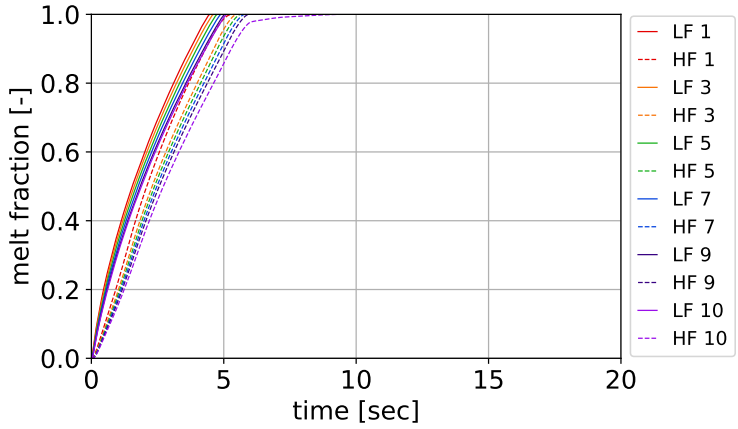

(a) The metal plate temperature at different locations plotted as a function of time.

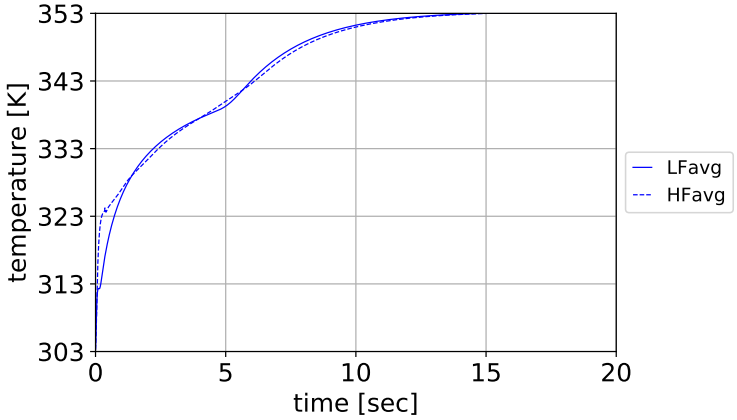

(b) The average metal plate temperature plotted as a function of time.

Figure 3.7. : Temporal and spatial comparison of the metal plate temperature for turbulent flow in the extended flat plate geometry.

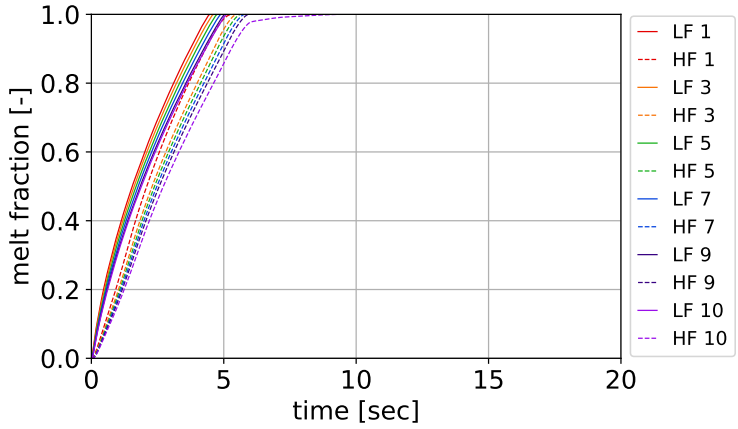

(a) The melt fraction of PCM at different locations plotted as a function of time.

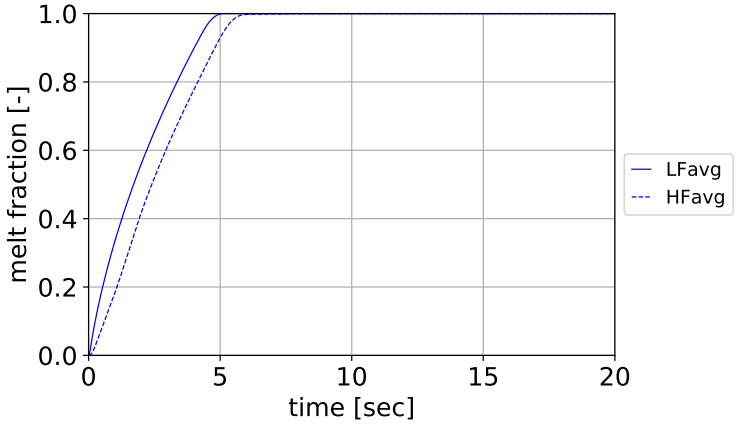

(b) The average melt fraction of PCM plotted as a function of time.

Figure 3.8. : Temporal and spatial comparison of the melt fraction of PCM for turbulent flow in the extended flat plate geometry.

Finally, as shown in Figure 3.9, the heat flux as predicted by the LF model is higher than that predicted by the HF model initially, with a NRMSE of 7%. Due to the higher heat flux, the PCM in the CPCM layer melts quicker as predicted by the LF model, as shown in Figure 3.8. Also, the initial fluid temperature as predicted by the LF model is lower than that predicted by the HF model, as shown in Figure 3.6. This may be a result of the turbulent heat transfer correlation lacking entry length considerations, which equates to the LF model treating the entry length as having a

fully developed thermal profile. Nevertheless, as was the case for laminar flow, we see that the transient behavior predicted by the LF model largely matches that of the HF model.

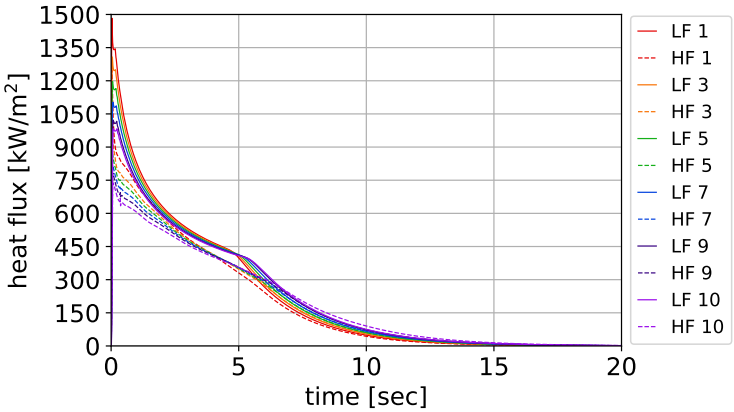

(a) The heat flux through fluid-metal plate interface at different locations plotted as a function of time.

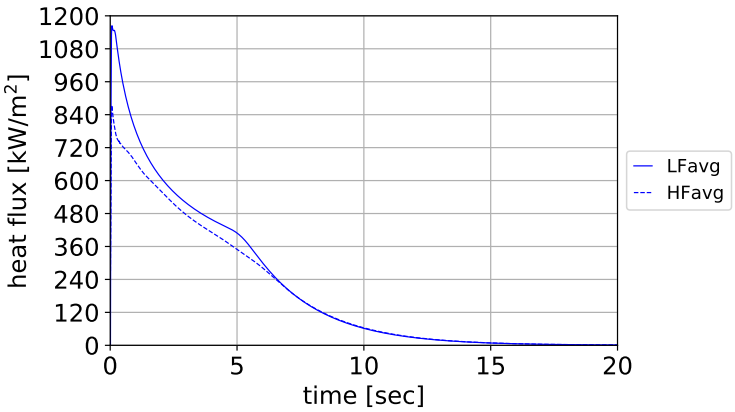

(b) The average heat flux through fluid-metal plate interface plotted as a function of time.

Figure 3.9. : Temporal and spatial comparison of the heat flux through the fluid-metal plate interface for turbulent flow in the extended flat plate geometry.

3.2.2 Cylindrical Tube Geometry

Here, I start by considering the laminar flow case for the cylindrical tube geometry and then move to the turbulent flow case. The radius of the fluid channel, the

thickness of the metal plate, the thickness of the CPCM layer and the length of the HX for laminar and turbulent flow cases are 0.5 mm, 1 mm, 1 cm and 10 cm, respectively.

Laminar Flow

In the case of laminar flow, the reduced-order model as well as the CFD ANSYS Fluent model were simulated for 200 seconds with a fluid velocity of 0.1 m/s. The number of fluid control volumes n_L considered in the reduced-order model was 70, and the number of CPCM sub-layers n_r considered was 50.

Figure 3.10 shows a comparison of the fluid temperature predicted by each model, both spatially and temporally. The transient fluid temperature trajectories predicted by the LF model generally match those predicted by the HF model, with a NRMSE of 3.5% in the magnitude of the fluid temperature between the two models.

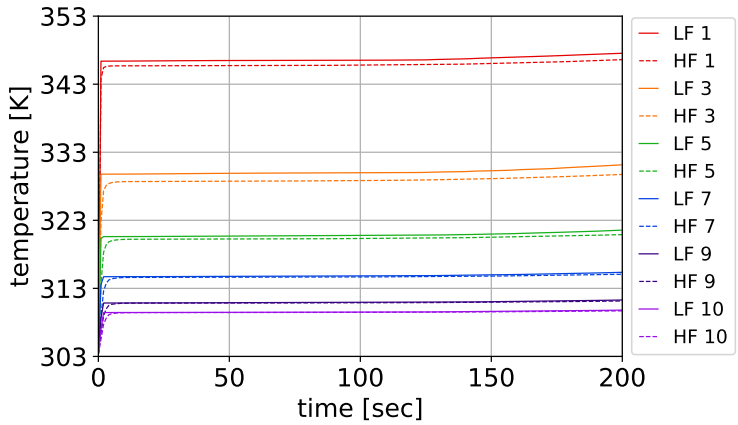

(a) The fluid temperature at different locations plotted as a function of time.

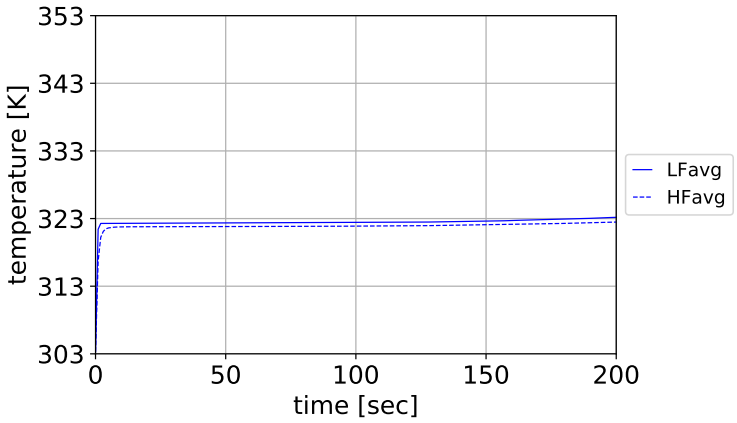

(b) The average fluid temperature plotted as a function of time.

Figure 3.10. : Temporal and spatial comparison of the fluid temperature for laminar flow in the cylindrical tube geometry.

Figure 3.11 and Figure 3.12 compare the metal plate temperature and the melt fraction of the PCM, respectively, as predicted by each model. The NRMSE in the magnitude of the metal plate temperature as predicted by each model is 2%. Furthermore, there is a NRMSE of 11% in the magnitude of the melt fraction across the CPCM layer.

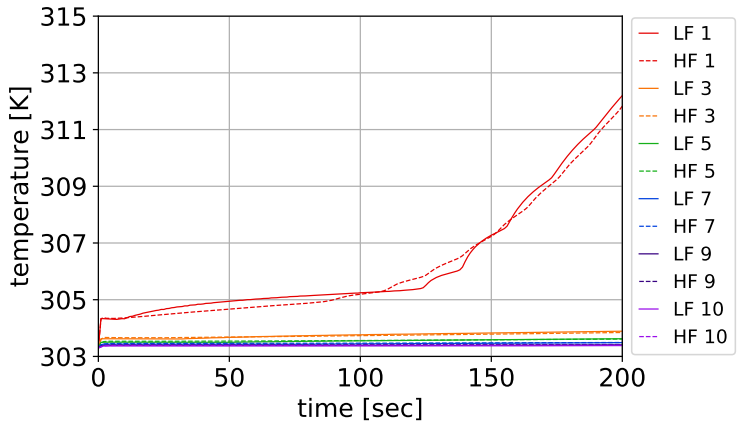

(a) The metal plate temperature at different locations plotted as a function of time.

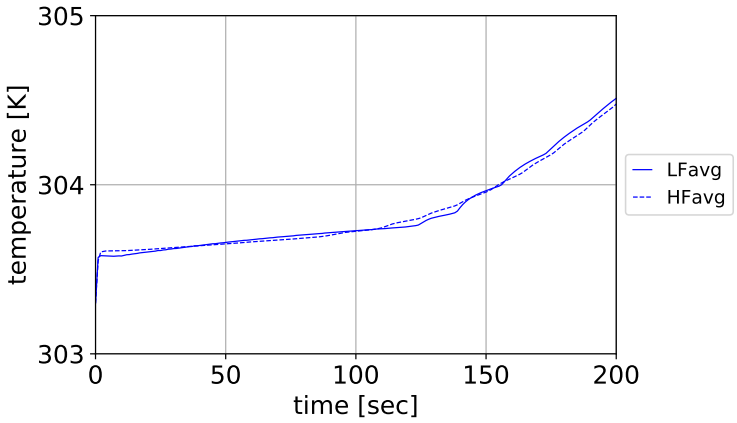

(b) The average metal plate temperature plotted as a function of time.

Figure 3.11. : Temporal and spatial comparison of the metal plate temperature for laminar flow in the cylindrical tube geometry.

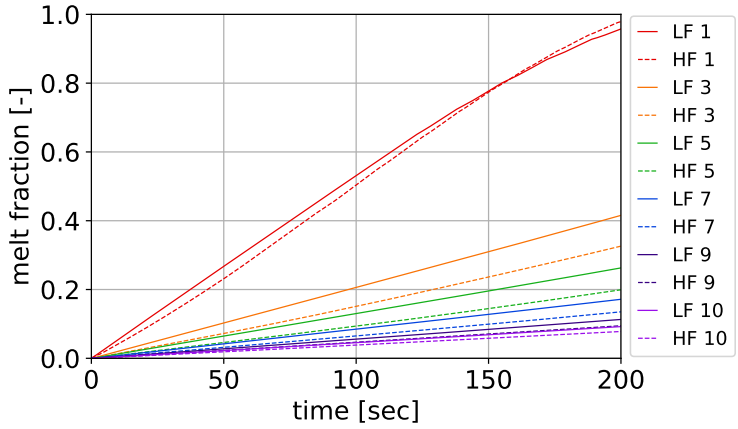

(a) The melt fraction of PCM at different locations plotted as a function of time.

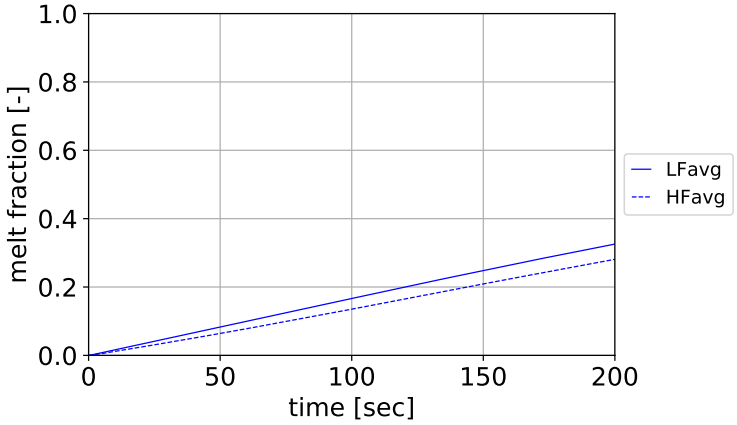

(b) The average melt fraction of PCM plotted as a function of time.

Figure 3.12. : Temporal and spatial comparison of the melt fraction of PCM for laminar flow in the cylindrical tube geometry.

Finally, there is an NRMSE of 9% in the magnitude of the heat flux, through the fluid-metal tube interface, between the two models. The heat flux across the fluid-metal plate interface predicted by the LF model is slightly higher than that predicted by the HF model, as shown in Figure 3.13. This is consistent with the melt fraction comparison shown in Figure 3.12, where the melt fraction of PCM as predicted by the LF model is higher than that predicted by the HF model which shows that the

heat absorbed by CPCM layer was higher in case of the LF model as compared to the HF model.

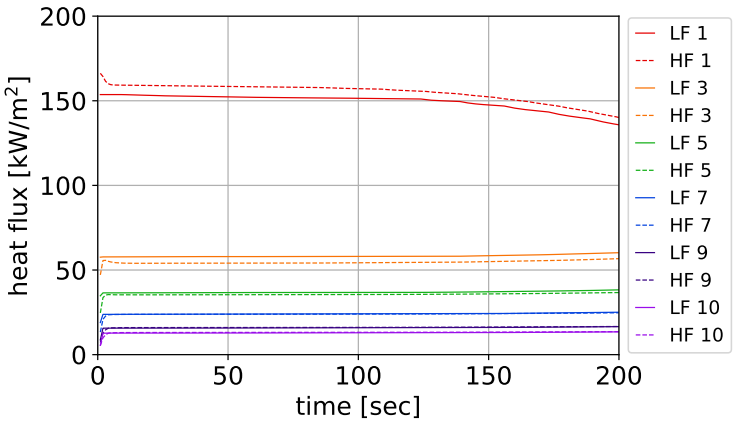

(a) The heat flux through the fluid-metal tube interface at different locations plotted as a function of time.

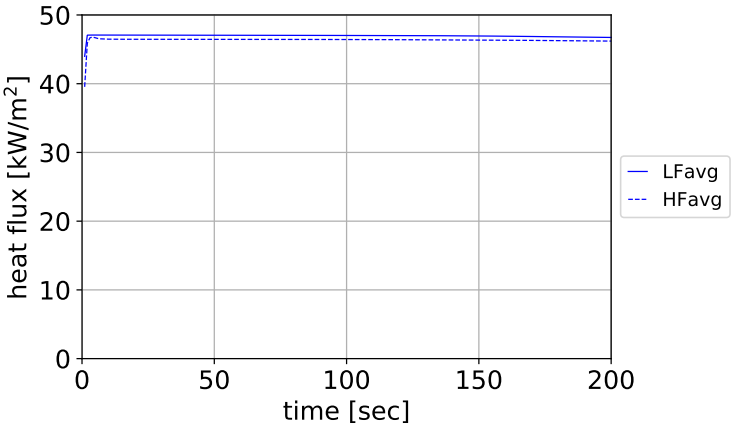

(b) The average heat flux through the fluid-metal tube interface plotted as a function of time.

Figure 3.13. : Temporal and spatial comparison of the heat flux through the fluid-metal tube interface for laminar flow in the cylindrical tube geometry.

Turbulent Flow

In the case of turbulent flow, both the models were simulated for 20 seconds and a fluid velocity of 4 meters per second. The number of fluid control volumes n_L

considered in the LF model was 70, and the number of PCM layers n_r considered was 50.

Figure 3.14 compares the fluid temperature predicted by each model. The NRMSE across the length of the fluid channel was calculated to be 0.8%.

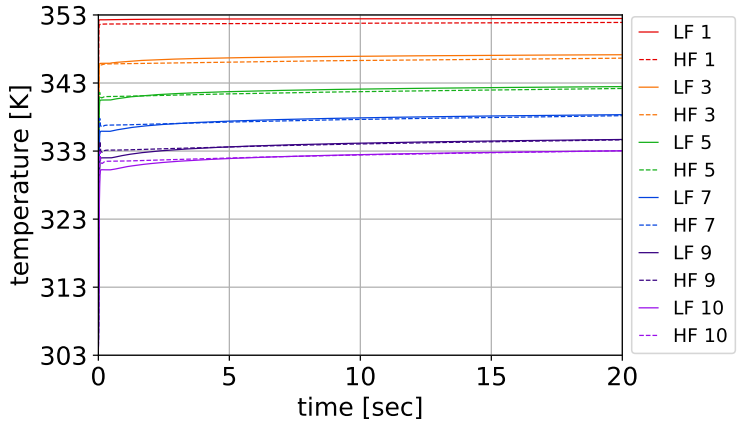

(a) The fluid temperature at different locations plotted as a function of time.

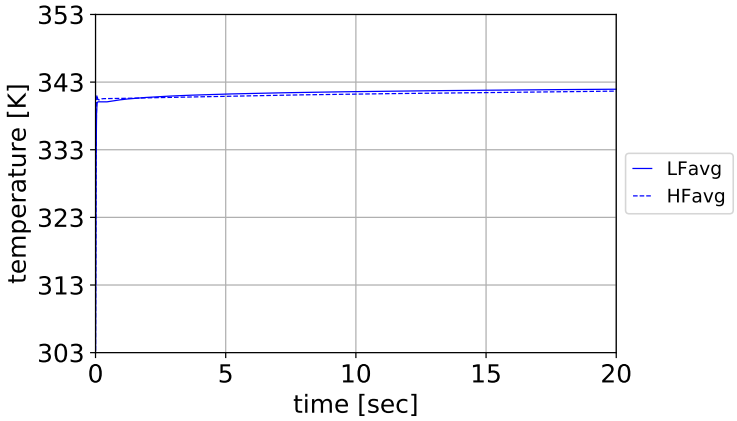

(b) The average fluid temperature plotted as a function of time.

Figure 3.14. : Temporal and spatial comparison of the fluid temperature for turbulent flow in the cylindrical tube geometry.

Figure 3.15 compares the temperature of the metal plate as predicted by each model, where the NRMSE is 7.7%. Figure 3.16 compares the melt fraction of PCM

within the CPCM layer as predicted by each model. The NRMSE in the magnitude of the melt fraction across the CPCM layer is 0.5%.

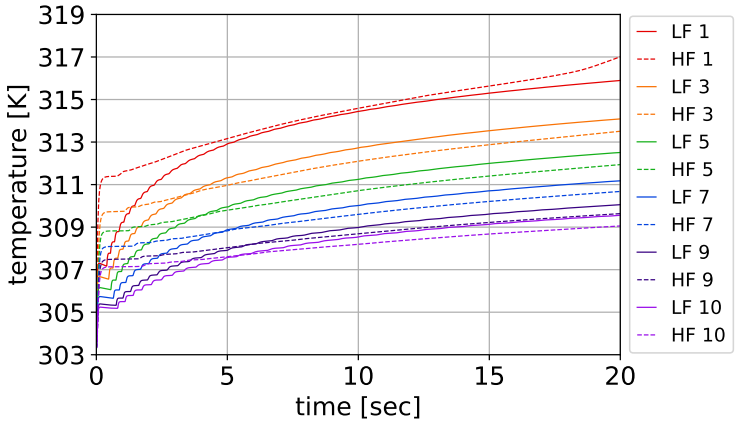

(a) The metal plate temperature at different locations plotted as a function of time.

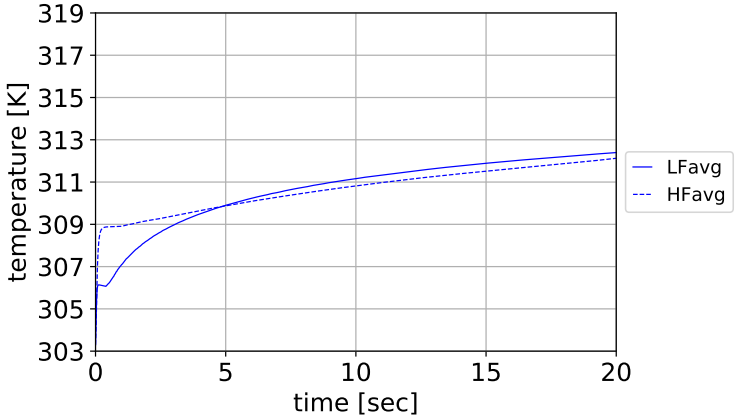

(b) The average metal plate temperature plotted as a function of time.

Figure 3.15. : Temporal and spatial comparison of the metal plate temperature for turbulent flow in the cylindrical tube geometry.

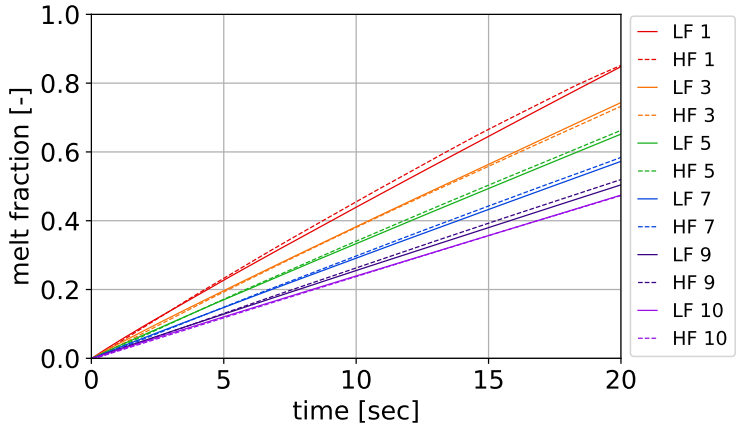

(a) The melt fraction of PCM at different locations plotted as a function of time.

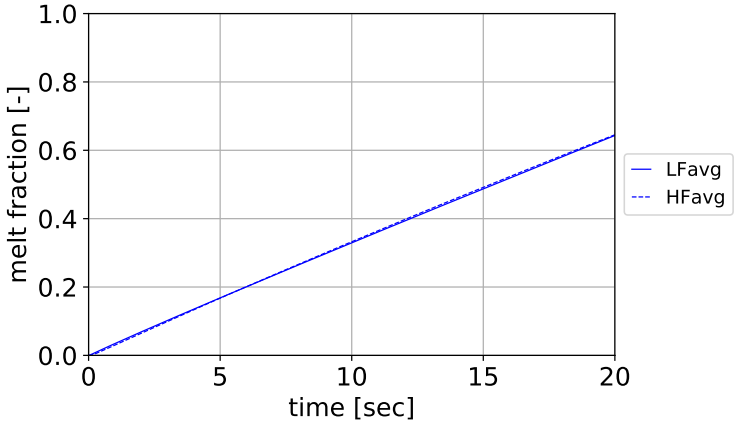

(b) The average melt fraction of PCM plotted as a function of time.

Figure 3.16. : Temporal and spatial comparison of the melt fraction of PCM for turbulent flow in the cylindrical tube geometry.

Finally, as shown in Figure 3.17, the heat flux as predicted by the LF model is consistently higher than that predicted by the HF model, with a NRMSE of 11%. Similar to the case of turbulent flow in the extended plate HX, this may be a result of the turbulent heat transfer correlation lacking entry length considerations, which equates to the LF model treating the entry length as having a fully developed thermal profile. Nevertheless, as was the case for laminar flow, I see that the transient behavior predicted by the LF model largely matches that of the HF model.

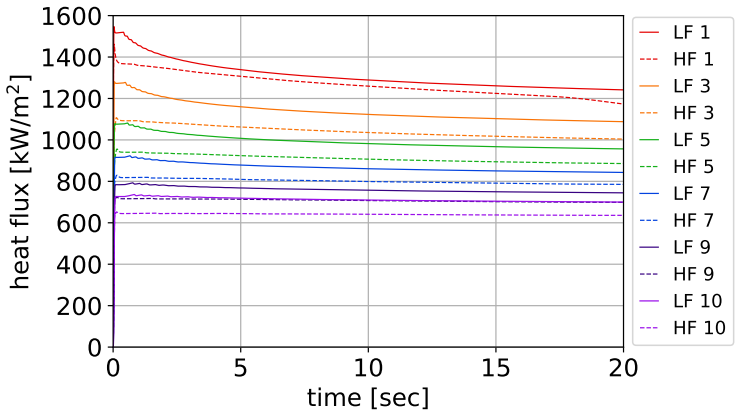

(a) The heat flux through fluid-metal tube interface at different locations plotted as a function of time.

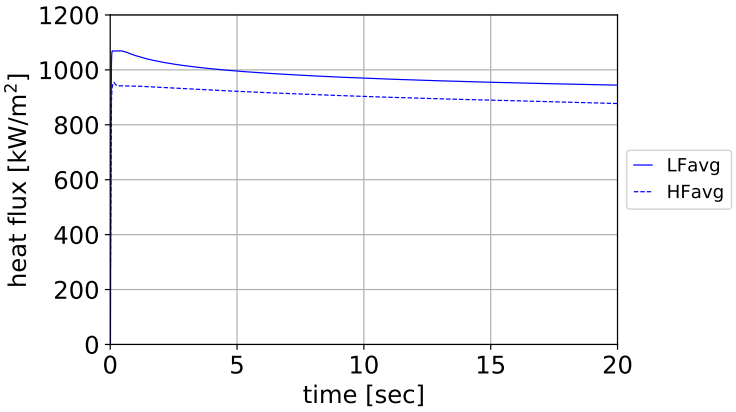

(b) The average heat flux through fluid-metal tube interface plotted as a function of time.

Figure 3.17. : Temporal and spatial comparison of heat flux through the fluid-metal tube interface for turbulent flow in the cylindrical tube geometry.

Table 3.3. : Summary of model validation - NRMSE values for laminar and turbulent fluid flow in both geometries.

State	**Plate (Laminar)**	**Plate (Turbulent)**	**Tube (Laminar)**	**Tube (Turbulent)**
Fluid temperature	1.9%	0.4%	3.5%	0.8%
Metal temperature	3.5%	2.4%	2%	7.7%
Melt fraction	2.8%	6.4%	11%	0.5%
Heat flux	7%	7%	9%	11%

Table 3.3 summarizes the validation results for both geometries under both turbulent and laminar flow regimes. The NRMSE values reported were calculated using the average temperature, the average melt fraction and the average heat flux evolution plots.

The reduced-order models were simulated using an Intel i5-8350U CPU with 16 GB memory (RAM) while the CFD models were simulated using an Intel i7-7700 CPU with 16 GB memory. The benchmark performance of the two CPU is similar and hence the simulation time using using the two CPU could be directly compared. The reduced-order model simulation takes up to 60 min, while the CFD model developed in ANSYS Fluent takes 12 hours. This shows that the reduced-order model is 12 times faster than the CFD model for the given choice of spatial discretization and time-step in reduced-order model simulation.

The model validation results presented in this chapter demonstrated the accuracy of the low fidelity model in predicting, both spatially and temporally, the evolution of different variables of interest such as the temperature of the fluid, the temperature of the metal separator, the melt fraction of PCM within the CPCM layer and the heat flux through the fluid-metal interface. The transient trajectories of the fluid temperature for the two models generally match with NRMSE error of less than 2% for the extended plate geometry and with NRMSE error of less than 4% for the cylindrical tube geometry. It should be noted that the total number of control volumes considered in each of these cases may be too large for some applications. Therefore, future work should explore the tradeoff between model accuracy and dynamic order.

4. PARAMETRIC STUDY

A parametric study can be used to understand the effects of a design parameter, or a combination of different design parameters, on any performance metric of interest. A list of possible design parameters and performance metrics that could be analyzed are listed in Table 4.1 and Table 4.2, respectively. In this chapter, I conduct such a study for the extended flat plate geometry to evaluate the effect of three design parameters—height of the CPCM layer, length of the HX, and volume fraction of metal in the CPCM layer—on the energy stored in the CPCM layer as well as energy stored in the CPCM layer per unit volume of the HX. I conduct an analogous study for the cylindrical tube geometry with the only difference being that *height* of the CPCM layer is replaced with *thickness*. I focus specifically on these three design parameters because they directly affect the amount of PCM present in the CPCM layer and hence the latent heat energy storage capacity of the HX. I fix the fluid channel height/radius as well as the height/thickness of the metal separator for each geometry, but these could be optimized in the future, subject to manufacturability or other design constraints. In fact, any of the other design variables or performance metrics listed in Tables 4.1 and 4.2, respectively, could be studied in the future.

Table 4.1. : List of design parameters that could be considered in a parametric study for the TES module.

Design Parameters
Length of the HX
Height/Radius of the metal plate
Height/Radius of the fluid channel
Height/Radius of the CPCM layer
Metal fraction by volume
Number of extended plate HXs stacked
Width of the extended plate HX

Table 4.2. : List of example performance metrics that could be considered in a parametric study for the TES module.

Performance Metrics
Power stored in the CPCM layer
Power per unit mass
Energy stored in the CPCM layer
Energy per unit volume
Energy per unit mass
Fluid exit temperature
Melt fraction of PCM

4.1 Extended Plate HX

Here, I conduct the parametric study for the extended plate HX. The fixed model parameters used in the study for this geometry are listed in Table 4.4.

Table 4.3. : List of fixed model parameters used in the parametric study.

Parameter	**Value**
simulated time (t_f)	10 s
time step (dt)	0.1 s
n_L	30
n_r	9
v_f	4 m/s
T_{in}	313.3 K
$T(0)$	303.3 K
T_m	303.3 K
h_p	1 mm
h_f	0.5 mm
d	20 cm

4.1.1 Single Variable Parametric Study

Here I conduct a parametric study of module geometry, specifically the height of the CPCM layer h_c and the length of the HX L and the metal fraction by volume within the CPCM layer ϕ on the energy stored in the CPCM layer E_c as well as energy stored per unit volume in the CPCM layer U_c over a fixed time period and with fixed fluid inlet temperature. These particular performance metrics of are of practical interest for applications involving TES modules. The material property values used for model simulation are the same as were presented in Table 3.2.

I first consider the effect of CPCM layer height on E_c and U_c; these results are summarized in Figure 4.1 and Figure 4.2, respectively. To generate the Parametric curves shown, $\phi = 0.5$ and $L = 30$ cm. Figure 4.1 shows that as the height of the CPCM layer increases, the energy stored in the CPCM layer increases but saturates at a CPCM layer height of approximately 5 mm. Increasing the CPCM layer height further would add mass and volume to the module without any contribution to its performance.

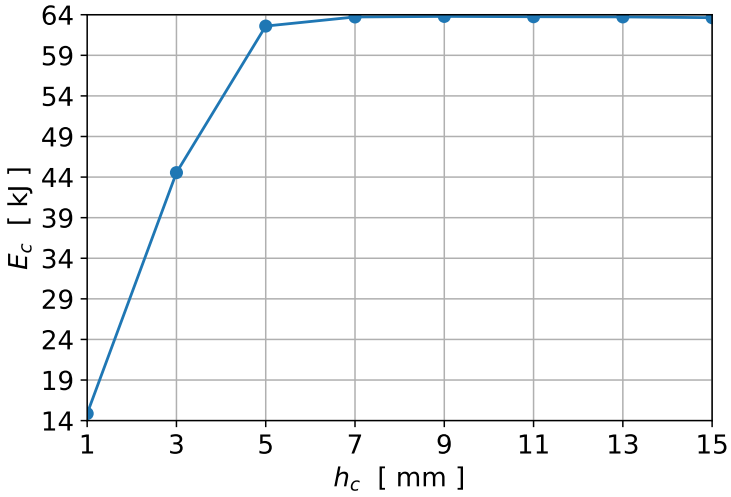

Figure 4.1. : Parametric plot showing the evolution of energy stored in the CPCM layer as a function of the height of the CPCM layer of the extended plate HX.

Figure 4.2 shows that as the height of the CPCM layer increases, the energy density also increases but reaches a maximum at a CPCM layer height of approximately 3 mm and then decreases in value. Increasing the height of the CPCM layer increases the heat storage capacity of the HX but that does not necessarily result in more energy stored. The rate of heat transfer from the working fluid to the CPCM layer depends on a number of factors, and Parametric curves such as these help in determining the upper limit of the total energy that can be extracted from a working fluid and the height of the CPCM layer at which the energy density is maximized.

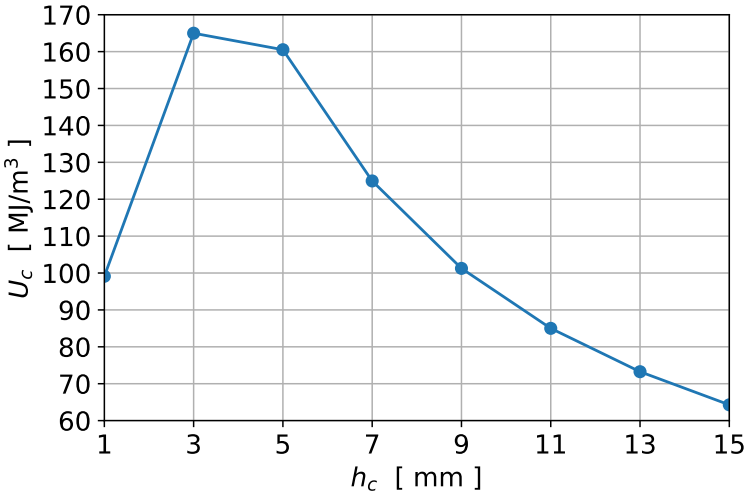

Figure 4.2. : Parametric plot showing evolution of energy density as a function of the height of the CPCM layer of the extended plate HX.

Next I consider the effect of variations in the HX length on the performance metrics of interest. For these simulations, $\phi = 0.5$ and $h_c = 1$ cm. Figure 4.3 shows that the energy stored in the CPCM layer does not scale linearly with the length of the HX. This is expected because as the fluid flows away from the inlet, the temperature of the fluid drops and hence, the heat transfer rate between the fluid and the CPCM layer decreases.

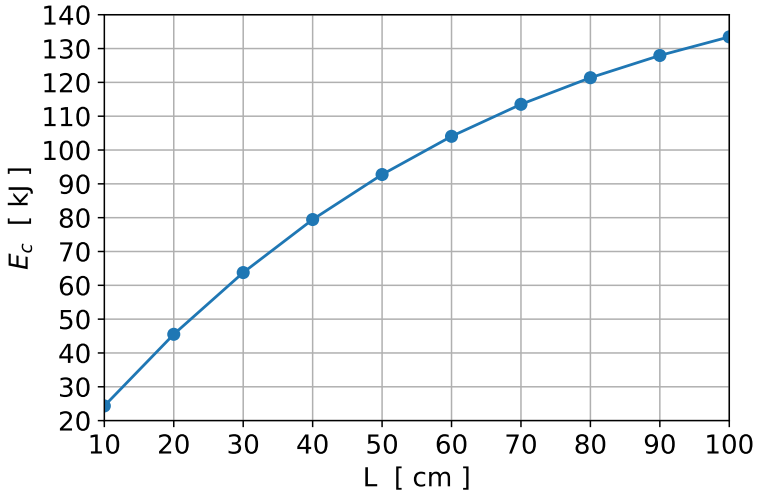

Figure 4.3. : Parametric plot showing evolution of energy stored in the CPCM layer as a function of the length of the extended plate HX.

The energy per unit volume decreases with an increase in the length of the HX, as shown in Figure 4.4. The total energy stored in the CPCM layer increases with increase in the length of the HX as shown in Figure 4.3 but the rate of increase in E_c is smaller than the rate of increase in the volume of the HX. This shows that there is a trade-off between the total energy stored in the CPCM layer and the volume density of that energy. For a different fluid inlet temperature, the Parametric curve for the energy density could attain a maximum and then start to decrease. Such a trend will occur when the rate of heat transfer from the working fluid to the CPCM layer increases faster than the rate at which the volume of the HX increases with increase in length. In summary, the Parametric curves show that similar to the height of the CPCM layer, the length of the HX helps to increase the total energy storage capacity of a HX, but the energy storage density decreases after a certain value of the parameter L.

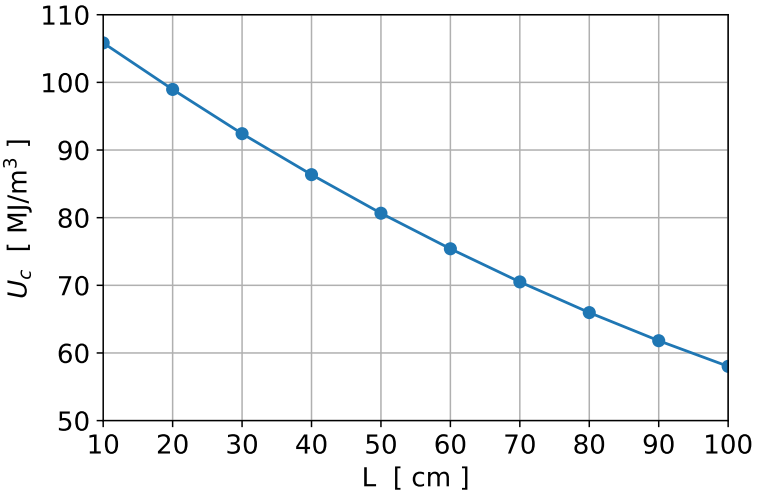

Figure 4.4. : Parametric plot showing evolution of energy per unit volume as a function of the length of the CPCM layer of the extended plate HX.

Finally, I vary the volume fraction of metal within the CPCM layer ϕ and quantify its effect on the energy stored in the CPCM layer E_c as well as the energy stored per unit volume in the CPCM layer U_c over a fixed period of time. The energy stored in the CPCM layer increases initially, attains a maximum at a metal fraction of approximately 0.5, and then starts to decrease, as shown in Figure 4.5. The initial increase in the energy stored is due to an increase in the effective thermal conductivity of the CPCM layer due to a higher metal fraction value. The increase in metal fraction also results in a decrease in the amount of PCM near the metal plate where melting occurs quickly because of the high heat transfer rate through the metal plate. In turn, the latent heat storage capacity of the CPCM layer decreases. Hence, there is a trade-off between the rate of heat transfer from the working fluid to the CPCM layer and the latent heat storage capacity of the CPCM layer. The effects of metal volume fraction on the energy storage density will be identical to the effects on the total energy stored because varying the metal fraction does not change the volume of the HX.

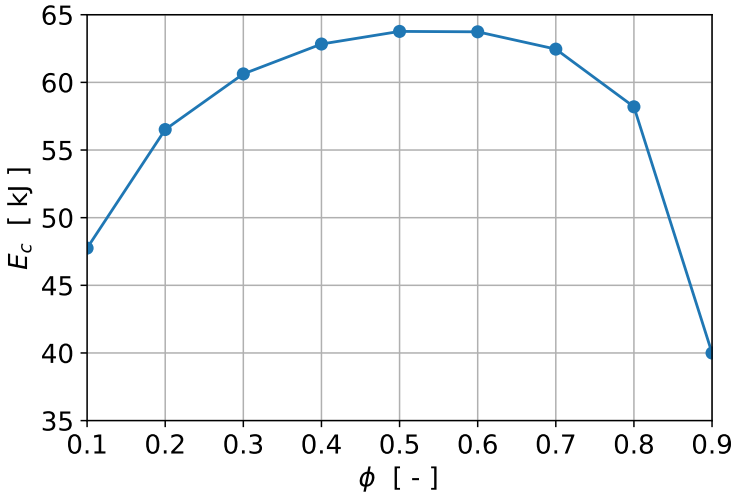

Figure 4.5. : Parametric plot showing the evolution of energy stored in the CPCM layer as a function of the metal fraction in the CPCM layer of the extended plate HX.

4.1.2 Multivariate Parametric Study

Here I consider the same design parameters as before, but evaluate their effect on the performance metrics of interest when varied two at a time. I first fix the HX length to be 30 cm and vary the CPCM layer height and metal volume fraction.

Figure 4.6 shows that the maximum energy density is achieved at a height of approximately 3 mm and at 0.3 volume fraction of metal in the CPCM layer, but a metal volume fraction of 0.3 does not result in optimal energy density for a different height of the CPCM layer. Thus, the optimal design configuration cannot be determined by optimizing individual parameters at a time and hence, multivariate parametric analysis should be used when optimizing multiple design parameters. The optimal CPCM layer height for achieving a maximum energy density increases with an increase in the volume fraction of metal. When the volume fraction of metal is increased, the volume of PCM in the CPCM layer decreases, and hence the latent heat energy storage capacity of the CPCM layer decreases. This decrease in the latent heat energy

storage capacity of the CPCM layer can be compensated by increasing the height of the CPCM layer thus, increasing the total volume of the PCM.

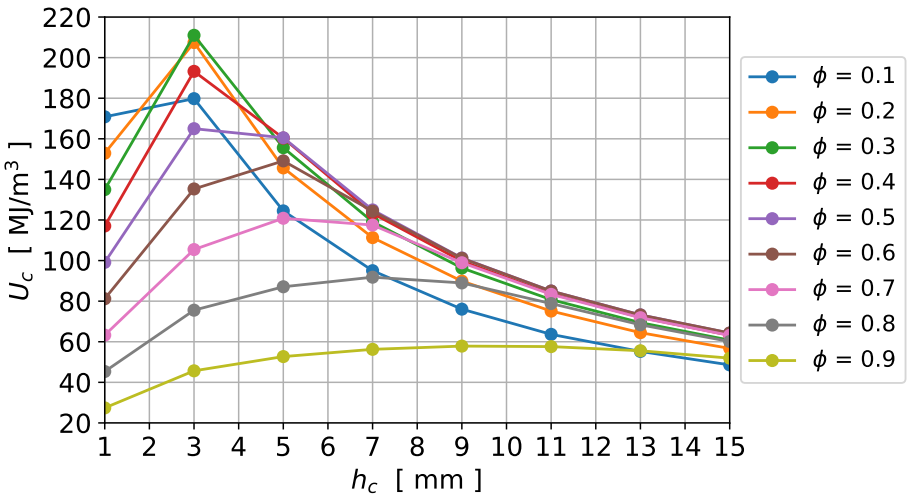

Figure 4.6. : Parametric plot showing evolution of energy density as a function of the height of the CPCM layer for different volume fraction values of metal within the CPCM layer of the extended plate HX.

Next I fix the metal volume fraction to be 0.5. Figure 4.7 shows that the maximum energy per unit volume is achieved at a CPCM layer height of 5 mm and HX length of 10 cm. The energy density for the HX with length 10 cm is expected to be higher than that for a HX with length more than 10 cm because the rate of increase in E_c with length is slower than the rate at which the volume of the HX increases. The optimal CPCM layer height decreases with an increase in the length of the HX. This is because as the HX length increases, the rate of increase in volume of the HX is reduced by decreasing the height of the CPCM layer. Since the energy density is inversely proportional to the volume of the HX, reducing the rate of increase in volume will help in achieving a higher energy density value.

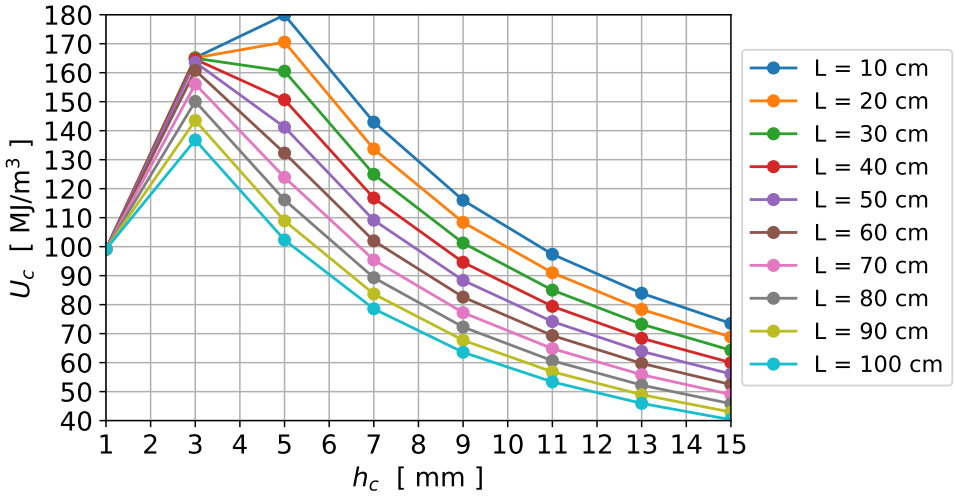

Figure 4.7. : Parametric plot showing evolution of energy per unit volume as a function of the height of the CPCM layer for different lengths of the extended plate HX.

Finally, I fix the CPCM layer height to be 1 cm. Figure 4.8 shows that the optimal energy density at any length of the HX is achieved when the volume fraction of metal is 0.6. The effective horizontal heat transfer coefficient of the CPCM layer is much smaller than the effective vertical heat transfer coefficient of the section of the CPCM layer because the thermal resistors of the PCM and the metal fins are in series for the horizontal direction heat transfer, while the thermal resistors of the PCM and metal fins are in parallel for the vertical direction heat transfer. Due to this, the rate of heat transfer in the direction of fluid flow within the CPCM layer is very small as compared to that from the working fluid to the CPCM layer. Now, as shown in Figure 4.6, the total volume of PCM in the CPCM layer decreases with increase in the value of ϕ and hence, the latent heat storage capacity of the CPCM layer decreases. But the increase in volume fraction of metal in the CPCM layer results in higher effective thermal conductivity of the CPCM layer. Due to this, the rate of heat transfer from the working fluid to the CPCM layer increases. Hence, there is a trade-off between the latent heat energy storage capacity of the CPCM layer and

the effective thermal conductivity of the CPCM layer when varying the metal volume fraction within the CPCM layer. The temperature difference between the fluid and the CPCM layer is highest near the inlet of the fluid channel and hence, it is important that CPCM near the inlet of the fluid channel have an optimal metal volume fraction so that both the effective thermal conductivity from the working fluid into the CPCM layer (effective vertical thermal conductivity) and the latent heat storage capacity are optimized. Since the metal is distributed uniformly within the CPCM layer for the parametric studies, the optimal metal volume fraction within the CPCM layer is primarily determined by the optimal metal volume fraction required within the section of the CPCM layer near the inlet of the fluid channel for an optimal rate of heat transfer near the inlet and is not very sensitive to the total length of the HX.

The effects of the trade-off between the latent heat storage capacity of the CPCM layer and the effective vertical thermal conductivity of the CPCM layer can be observed when the curves for $\phi = 0.3$ and $\phi = 0.8$ are analyzed. For a HX with length 10 cm, the case with $\phi = 0.3$ has a higher energy density as compared to the case with $\phi = 0.8$. But, at a HX length of 100 cm, the case with $\phi = 0.8$ has a slightly higher energy density as compared to the case with $\phi = 0.3$. This is because for $\phi = 0.8$ and L =10 cm, the latent heat storage capacity of the CPCM layer is low as compared to the case when $\phi = 0.3$ and L =10 cm. Hence, there is less PCM in the volume to melt and store energy in form of latent heat energy. So the energy density is higher for the HX with $\phi = 0.3$ and L =10 cm. However, when the length of the HX is 1 m, both HXs, with $\phi = 0.3$ and with $\phi = 0.8$, have enough volume of PCM to melt and store the heat extracted from the working fluid in the form of latent heat energy. Therefore, the case with a higher effective thermal conductivity of the CPCM layer has slightly better energy storage density.

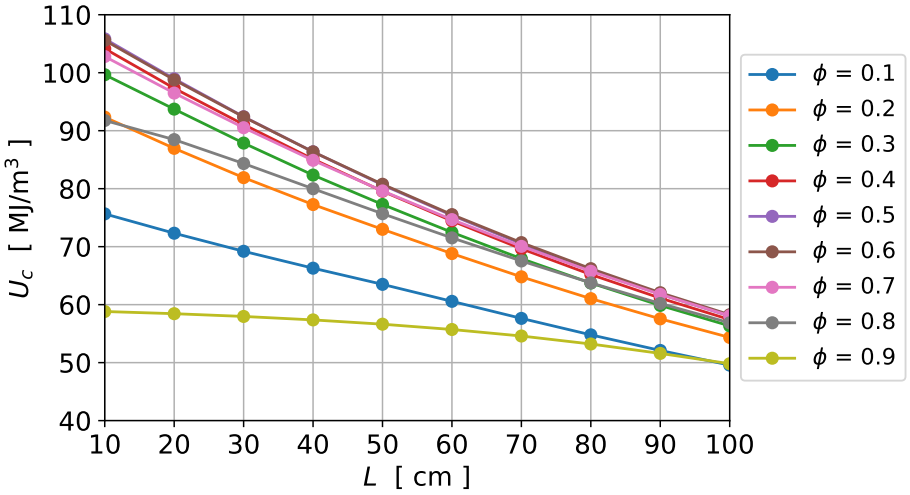

Figure 4.8. : Parametric plot showing evolution of energy per unit volume as a function of the length of the HX for different volume fraction values of metal within the CPCM layer of the extended plate HX.

4.2 Cylindrical Tube HX

Here, I conduct the parametric study for the cylindrical tube HX. The list of fixed model parameters used in the parametric studies for the cylindrical tube HX are shown in Table 4.4.

Table 4.4. : List of fixed model parameters used in the parametric studies.

Parameter	**Value**
simulated time (t_f)	100 s
time step (dt)	0.5 s
n_L	30
n_r	10
v_f	4 m/s
T_{in}	313.3 K
$T(0)$	303.3 K
T_m	303.3 K
t_p	1 mm
r_f	0.5 mm

4.2.1 Single Variable Parametric Study

Here, I conduct a parametric study of the cylindrical tube module geometry, specifically the thickness of the CPCM layer t_c, the length of the HX L and the metal fraction by volume within the CPCM layer ϕ on the energy stored in the CPCM layer E_c as well as energy stored per unit volume in the CPCM layer U_c over a fixed time period and with fixed fluid inlet temperature. The material property values used for this analysis are the same as were presented in Table 3.2.

I first consider the effects of CPCM layer thickness on E_c and U_c; these results are summarized in Figure 4.9 and Figure 4.10, respectively. To generate the Parametric curves shown, I let $\phi = 0.5$ and $L = 30$ cm. Figure 4.9 shows that as the thickness of the CPCM layer increases, the energy stored in the CPCM layer increases but saturates at a CPCM layer thickness of approximately 7 mm. Increasing the CPCM layer thickness further would add mass and volume to the module without any contribution to its performance.

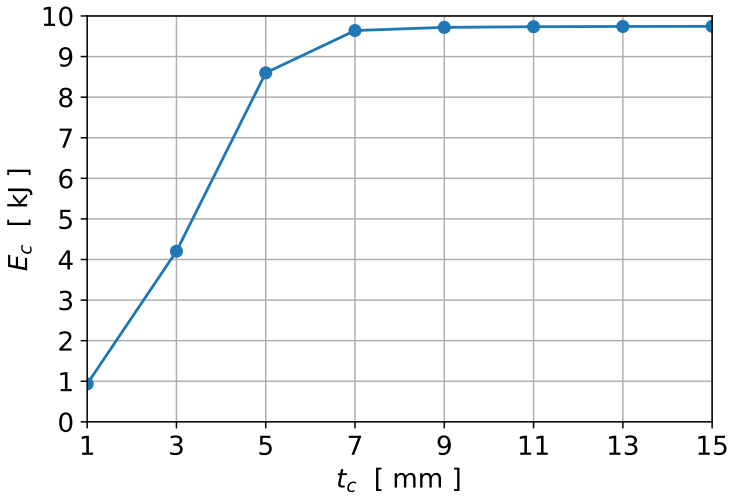

Figure 4.9. : Parametric plot showing the evolution of energy stored in the CPCM layer as a function of the thickness of the CPCM layer of the cylindrical tube HX.

Figure 4.10 shows that as the thickness of the CPCM layer increases, the energy density also increases but reaches a maximum at a CPCM layer thickness of approximately 3 mm and then decreases in value. The effects of the CPCM thickness on the cylindrical tube HX are similar to the effects of the CPCM layer height on the extended plate HX. Increasing the CPCM layer thickness increases the heat storage capacity of the layer but it does not necessarily result in a higher heat energy stored because the total heat that could be extracted from the working fluid depends on many other factors including the fluid inlet temperature. The increase in thickness of the CPCM layer after E_c reaches saturation would be useful if the inlet temperature of the fluid increases which in turn increases the rate of heat transfer from the working fluid to the CPCM layer.

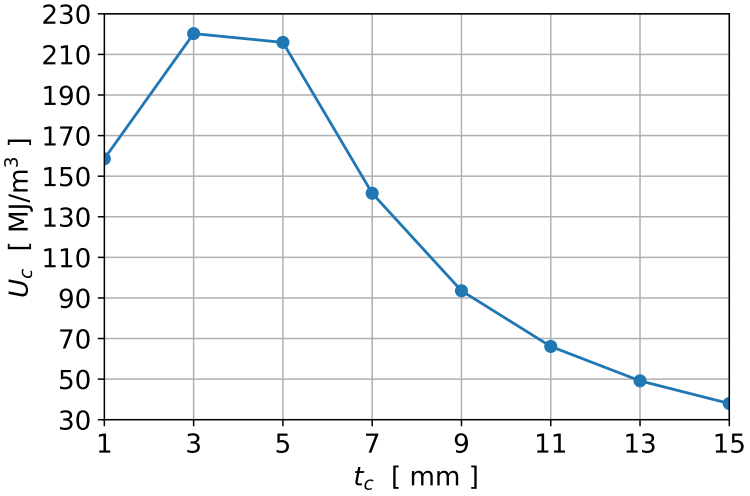

Figure 4.10. : Parametric plot showing evolution of energy per unit volume as a function of the thickness of the CPCM layer of the cylindrical tube HX.

Next I consider the effect of varying HX length on the performance metrics of interest. For these simulations, $\phi = 0.5$ and $t_c = 1$ cm. Figure 4.11 shows that the energy stored in the CPCM layer does not scale linearly with the length of the HX. This is expected because as the fluid flows away from the inlet, the temperature of the

fluid drops and hence, the heat transfer rate between the fluid and the CPCM layer decreases. Note that the length of the HX is varied up to 150 cm for this parametric study to show the length at which E_c starts to saturate. Elsewhere I vary the HX length up to $L = 100$ cm.

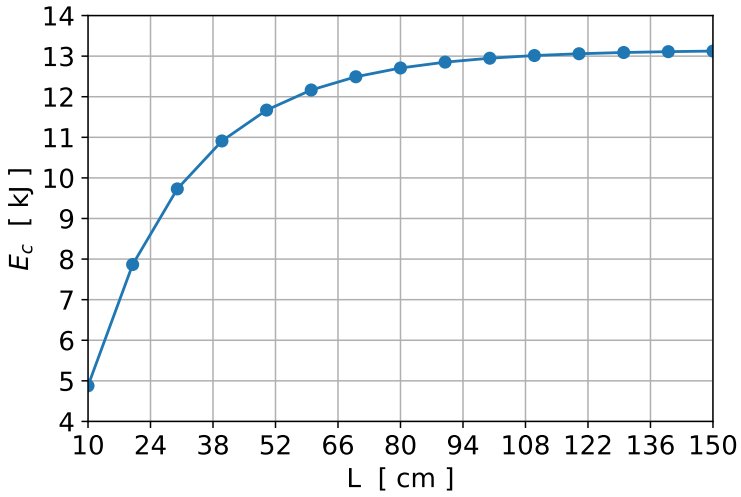

Figure 4.11. : Parametric plot showing evolution of energy stored in the CPCM layer as a function of the length of the CPCM layer of the cylindrical tube HX.

The energy density decreases with an increase in the HX length, as shown in Figure 4.12. Similarly, the total energy *stored* in the CPCM layer increases with increasing HX length as shown in Figure 4.11, but the rate of increase in E_c is lower than the rate of increase in the volume of the HX. The effects of the length of the HX on the performance metrics for the cylindrical tube HX are again similar to that observed in the extended flat plate geometry. There is a trade-off between the total energy stored in the CPCM layer and the volume density of that energy. As seen in Figure 4.8 for the extended plate geometry, the trade-off between energy stored and energy storage density can be overcome by decreasing the thickness of the CPCM layer when the length is increased so as to keep the total volume of the HX low. This will be discussed in detail in Section 4.2.2.

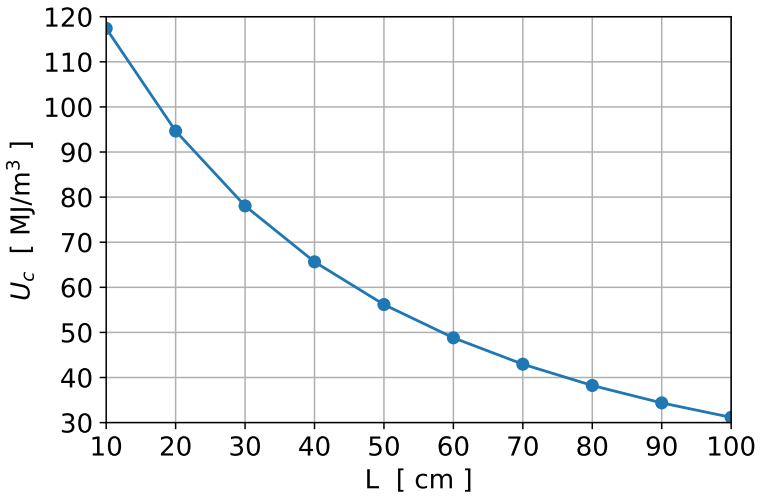

Figure 4.12. : Parametric plot showing evolution of energy per unit volume as a function of the length of the CPCM layer of the cylindrical tube HX.

Finally, I vary the volume fraction of metal within the CPCM layer and quantify its effects on the energy stored in the CPCM layer, E_c, as well as the energy density, U_c, over a fixed period of time. The energy stored in the CPCM layer increases initially, attains a maximum at around $\phi = 0.7$, and then starts to decrease, as shown in Figure 4.13. Again, the reason for this behavior is the same as that explained for the Parametric curve shown in Figure 4.5, for the extended plate geometry. Due to the trade-off between the rate of heat transfer from the working fluid to the CPCM layer and the latent heat energy storage capacity of the CPCM layer, the energy density curve is concave with a unique global maximum.

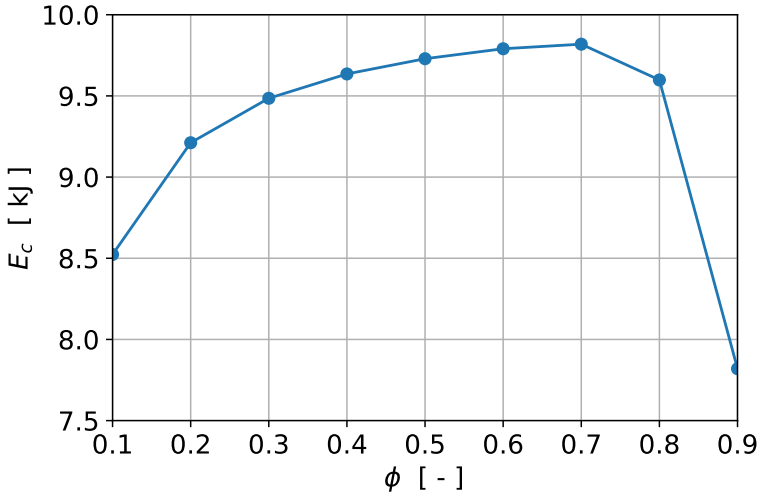

Figure 4.13. : Parametric plot showing the evolution of energy stored in the CPCM layer as a function of the metal fraction in the CPCM layer of the cylindrical tube HX.

4.2.2 Multivariate Parametric Study

Here I consider the same design parameters as before, but evaluate their effects on the performance metrics when varied two at a time. I first fix the HX length to be 30 cm and vary the CPCM layer thickness and metal volume fraction. Figure 4.14 shows that the maximum energy density is achieved at a CPCM layer thickness of approximately 3 mm and at 0.1 volume fraction of metal in the CPCM layer. However, a metal volume fraction of 0.1 does not result in optimal energy density for a different thickness of the CPCM layer. The optimal CPCM layer thickness increases with increase in the value of ϕ. The reason for this behavior for the cylindrical tube geometry is same as that for the extended plate geometry which is described in Subsection 4.1.2.

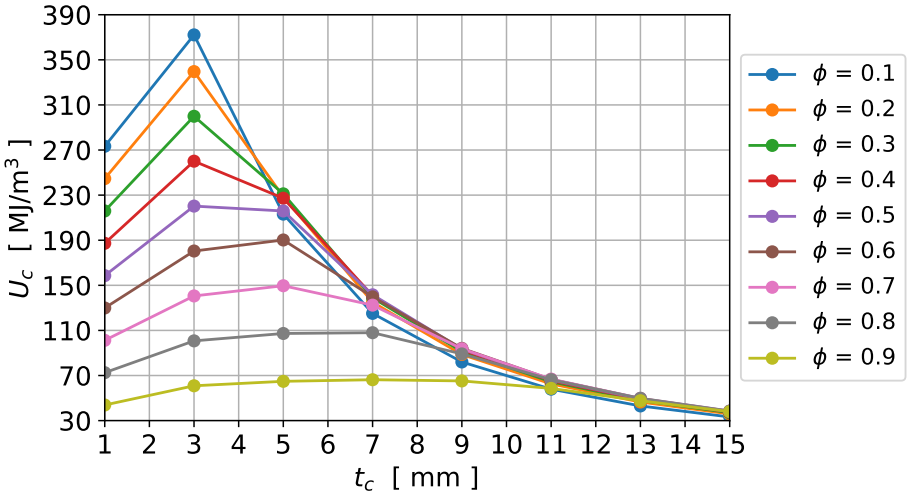

Figure 4.14. : Parametric plot showing evolution of energy per unit volume as a function of the thickness of the CPCM layer for different volume fraction of metal within the CPCM layer of the cylindrical tube HX.

Next I fix the metal volume fraction to be 0.5. Figure 4.15 shows that the maximum energy per unit volume is achieved at a CPCM layer thickness of 5 mm with a HX length of 10 cm. The energy density for the HX with a length of 10 cm is expected to be higher than that for a HX with length more than 10 cm because the rate of increase in E_c as a function of length is less than the rate at which the volume of the HX increases. The optimal CPCM layer thickness decreases with increase in the length of the HX. This is because the rate of increase in volume of the HX, due to increase in the length of the HX, decreases with decrease in the thickness of the CPCM layer which is favourable for optimizing the energy density because the energy density is inversely proportional to the volume of the HX.

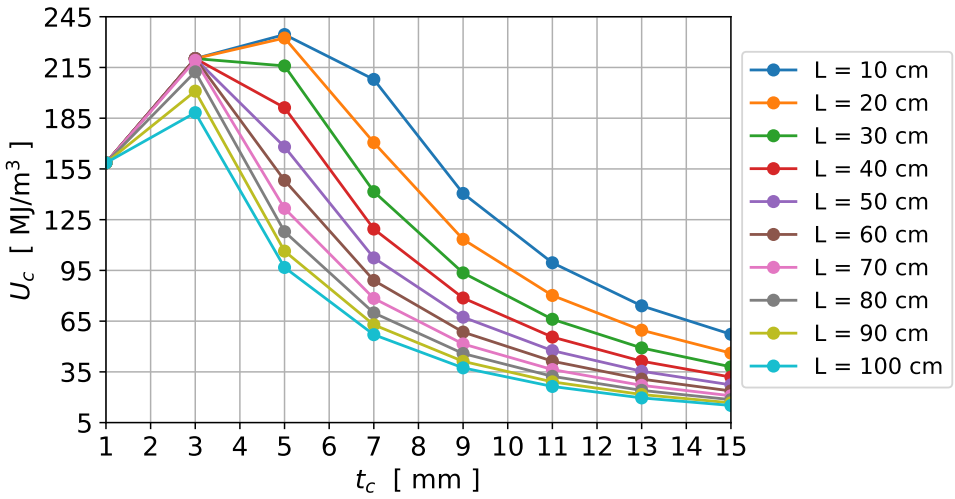

Figure 4.15. : Parametric plot showing evolution of energy per unit volume as a function of the thickness of the CPCM layer for different lengths of the cylindrical tube HX.

Finally I fix the CPCM layer thickness to 1 cm and vary the length of the HX as well as the metal volume fraction within the CPCM layer. Figure 4.16 shows that the optimal energy density at any HX length is achieved at $\phi = 0.7$. The optimal metal volume fraction does not change with the length of the HX due to the same reason as explained in Section 4.1.2, for the Parametric curve shown in Figure 4.8. It can be observed from the Parametric curve that for the energy density at HX length of 10 cm, the HX with $\phi = 0.2$ has a higher U_c value as compared to the HX with $\phi = 0.8$. But for the HX length of 20 cm or higher, the HX with $\phi = 0.8$ has a slightly higher energy density value as compared to the HX with $\phi = 0.2$. Again, the reason for this is the same as that explained in Subsection 4.1.2 for the extended plate HX.

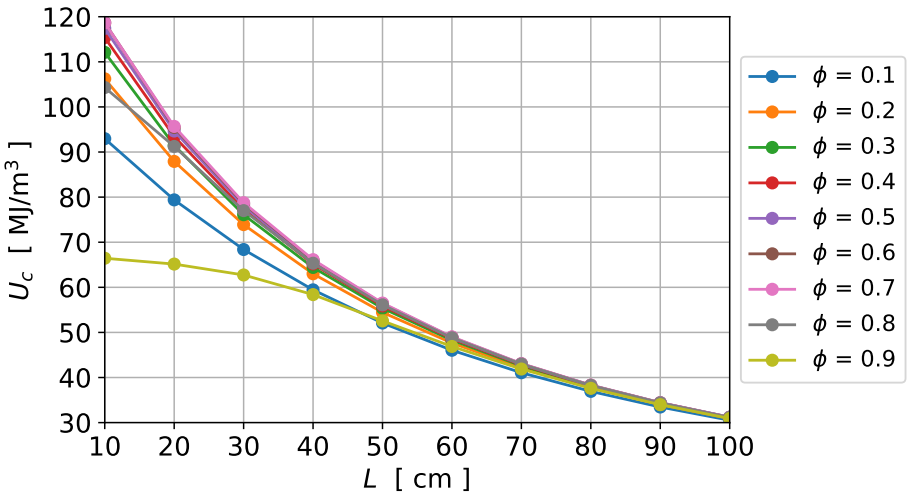

Figure 4.16. : Parametric plot showing evolution of energy per unit volume as a function of the length of the HX for different volume fraction values of metal within the CPCM layer of the cylindrical tube HX.

4.3 Summary

The single variable parametric study results for the extended plate geometry show that the energy stored in the CPCM layer increases with an increase in the length of the HX or in the height of the CPCM layer. The value of E_c increases initially, attains a maximum, and then starts to decrease as the metal volume fraction increases. The increase in the energy storage density is not directly proportional to the increase in the module dimensions considered in the study due to which, the energy density does not increase consistently with an increase in length of the HX or the height of the CPCM layer. The trends in the results for the cylindrical tube HX are identical to those in the results for the extended plate geometry. The multivariate parametric study results for both geometries show that the optimal energy density is achieved when the total volume of PCM melted within the CPCM layer is maximized. The total volume of PCM that melts during an operation depends on the trade-off between the effective thermal conductivity of the CPCM layer and the amount of PCM available

to quickly melt near the metal separator. The optimal value of the volume of the PCM required to achieve an optimal energy density depends on factors such as the fluid inlet temperature, metal separator thickness, and the simulated time period, which were not varied here but should be considered in future work.

Parametric studies like those conducted here are are useful in determining an optimal design configuration when the number of design parameters to be optimized is relatively small (e.g. one to three). This method quickly becomes very complicated as the number of design parameters increases. An alternative approach is to use numerical optimization to find optimal module designs with a large number of design variables. In the next chapter, I present design optimization case studies in which up to 21 design parameters are optimized simultaneously to find a configuration that maximizes a particular performance metric for a given HX geometry.

5. MODULE DESIGN OPTIMIZATION

One of the primary reasons for developing a reduced-order model is to enable rapid optimization of system designs to meet various performance criteria. In this chapter I demonstrate this through a case study for each of the two geometries considered in this thesis. The specific design problem under consideration for both geometries is the maximization of the rate of heat extracted from the working fluid per unit mass of the module.

5.1 Extended Plate HX Geometry

In the case of the extended plate geometry, I consider four design variables: volume fraction of metal in the CPCM layer, ϕ, distributed spatially across the CPCM layer as shown in Figure 5.1, the height of the CPCM layer, h_c, the number of heat exchangers stacked on each other, N, and the depth of the module d. To model a non-uniform distribution of metal fraction within the CPCM layer, I consider 18 volumes, each with its own metal fraction ϕ_i, as shown in Figure 5.1. Note that these 18 volumes are not identical to the control volumes defined within the model for the purpose of simulating the dynamics of the HX.

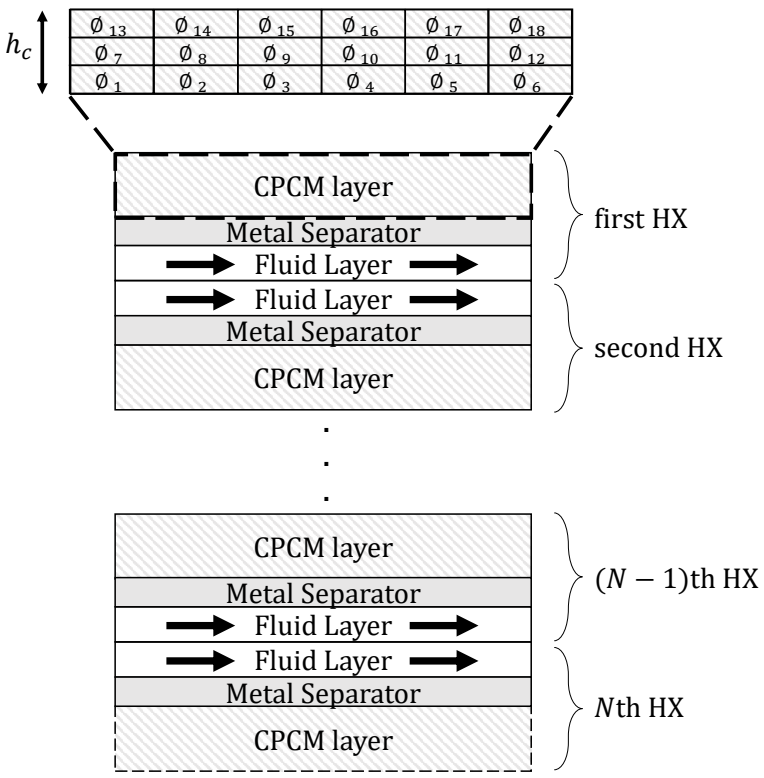

Figure 5.1. : Extended plate HX with 18 volumes defined within the CPCM layer to be optimized.

All of the fixed parameters used to simulate the model at each iteration of the optimization are given in Table 5.1. The design optimization problem is defined in Equation 5.1 where $x_d = \begin{bmatrix} \phi_1 & \phi_2 & \dots & h_c & N \end{bmatrix}^T$, and $u = \begin{bmatrix} v_f & T_{in}^f & T(0) \end{bmatrix}^T$.

$$
\begin{aligned}
\min_{x_d} \quad & J\left(\boldsymbol{x_d}\right) = -\left(\frac{\sum_{i=1}^{n_r n_L} m_{c,i} c_{p,i} \left(T_{c,i}\left(t_f\right) - T_{c,i}(0)\right) + \left(\sum_{i=1}^{n_r n_L} m_{c,i}\right) L_{fus}}{NLd\left(\rho_c h_c + \rho_f h_f + \rho_p h_p\right) t_f}\right) \\
\text{s.t.} \quad & NLd\left(h_c + h_p + h_f\right) = 4 \times 10^{-3}\text{m}^3 \\
& 0.01 \leq \phi_i \leq 0.99 \\
& 1\text{mm} \leq h_c \leq 15\text{mm} \\
& 1 \leq N \leq 20 \\
& \dot{x} = f(x_d, u)
\end{aligned}
\tag{5.1}
$$

Table 5.1. : List of fixed parameters used in the optimization case study.

Parameter	**Value**
simulated time (t_f)	10 s
time step (dt)	0.1 s
L	30 cm
n_L	30
n_r	9
v_f	4 m/s
T_{in}	313.3 K
$T(0)$	303.3 K
T_m	303.3 K
h_p	1 mm
h_f	0.5 mm
d	20 cm

The optimization problem is solved using the nonlinear optimization algorithm sequential quadratic programming (SQP) with multi-start [20]. SQP solves a sequence of optimization problems by optimizing the quadratic approximation of the cost function, subject to the linearized approximation of the constraints, to find a local optimum. The reduced-order model is wrapped in a function which takes as an input the vector of decision variables under consideration. The function returns

an array containing the cost function and constraints. The SQP algorithm calls this function iteratively until it converges to an optimum value based upon a user-defined convergence tolerance of 10^{-5} W/kg on the cost function. It should be noted that the number of heat exchangers, N, stacked to form a module must be an even integer. However, defining N as an integer in the optimization problem would require the use of mixed-integer programming. To avoid this additional complexity, the following procedure is used to make sure that N is an even integer:

1. Find an optimal design assuming N as a Real number (design vector $x_d = \begin{bmatrix} \phi_1 & \phi_2 & \dots & h_c & N \end{bmatrix}^T$).

2. Find the closest even integer to the optimal N by first dividing N by 2, rounding the value to the nearest integer, and then multiplying that value by 2.

3. Redefine the optimization problem using the reduced design vector $x_{d,red} = \begin{bmatrix} \phi_1 & \phi_2 & \dots & h_c \end{bmatrix}^T$ that now excludes N, and find a new optimal design.

In order to quantify the benefit of a non-uniform spatial distribution of metal within the CPCM layer, I compare results of the non-uniform spatial distribution case against a case when the TES module is optimized with a uniform distribution of metal. The optimal number of HXs, the optimal height of the CPCM layer and the optimal value of average metal fraction by volume in the CPCM layer for the two cases are given in Table 5.2. The average metal volume fraction within the CPCM layer is denoted by $\bar{\phi}$. The exact distribution of metal fraction by volume in percentage within the composite PCM layer for the case with non-uniform metal distribution is shown in Figure 5.2. The optimal distribution of metal fraction by volume within the CPCM layer is such that the CPCM sub-layer directly in contact with the metal separator has a higher metal fraction as compared to the second and the third CPCM sub-layers, and the second CPCM sub-layer has a higher metal fraction as compared

to the third sub-layer. The energy stored in the CPCM layer is maximized when the melt fraction of PCM within the CPCM layer is maximized because the PCM has a high latent heat storage capacity. In order for the melt fraction of the PCM within the CPCM layer to be as large as possible for the given simulation parameters, the rate of heat transfer in the direction perpendicular to the fluid flow should be high so that the PCM in the CPCM sub-layers away from the hot fluid starts to melt. This is achieved when the rate of heat transfer from the first CPCM sub-layer to the second sub-layer is high which can be achieved by having a higher metal fraction by volume in the first CPCM sub-layer as compared to the second and the third sub-layer. Similarly, the metal fraction by volume should be higher in the second sub-layer as compared to the third sub-layer.

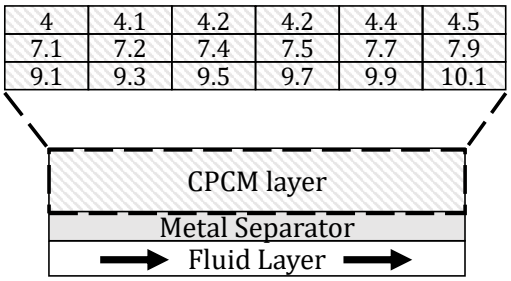

Figure 5.2. : Optimal metal distribution (in percent metal by volume) within the CPCM layer to maximize the power per unit volume performance measure.

Table 5.2. : Optimization results for uniform and non-uniform distribution of metal fraction by volume within the CPCM layer.

Variable	**Optimal Value** (Uniform Distribution)	**Optimal Value** (Non-uniform Distribution)
N	8	8
h_c	6.83 mm	6.83 mm
ϕ or $\bar{\phi}$	ϕ =7.7 %	$\bar{\phi}$ =7.1 %
P/m	2.09 kW/kg	2.12 kW/kg
P	14183.8 W	14281.5 W
m	6.772 kg	6.479 kg

Thus, by allowing for non-uniform spatial variation of the metal composition within the CPCM layer, the power per unit mass increased by 1.24% while the mass of the system decreased by 0.4%, as compared to the case with metal distributed uniformly throughout the CPCM.

An important question is how sensitive the optimization results are to the level of spatial discretization considered in the design problem. To examine this, the optimization problem was solved for 6 different cases. Let the number of sections in the direction of fluid flow be indicated by s_x and the number of sub-layers of the CPCM layer be indicated by l_y. The first case considered to generate the Pareto curve shown in Figure 5.3 was with $s_x = 1$ and $l_y = 1$, resulting in 1 volume considered within the CPCM layer. The second case was with $s_x = 4$ and $l_y = 2$, resulting in 8 total volumes considered within the CPCM layer. The third case was with $s_x = 5$ and $l_y = 3$, resulting in 15 total volumes within the CPCM layer. The fourth case was with $s_x = 6$ and $l_y = 3$, resulting in 18 total volumes within the CPCM layer. The fifth case had $s_x = 8$ and $l_y = 4$, resulting in 32 volumes within the CPCM layer. The last case had $s_x = 9$ and $l_y = 4$, resulting in 36 volumes within the CPCM layer. The results are summarized using a Pareto curve that characterizes the change in the power per unit mass as a function of the level of spatial discretization of the metal within the CPCM layer, as shown in Figure 5.3. It is clear that as the spa-

tial discretization increases, the power per unit mass also increases initially and then starts to saturate. This shows that the performance metric would start to saturate at a certain number of volumes considered within the CPCM layer, with independent metal volume fraction ϕ_i, and increasing the spatial discretization further would not improve the performance metric. Increasing the spatial discretization further would add complexity to the design problem without any contribution to the performance.

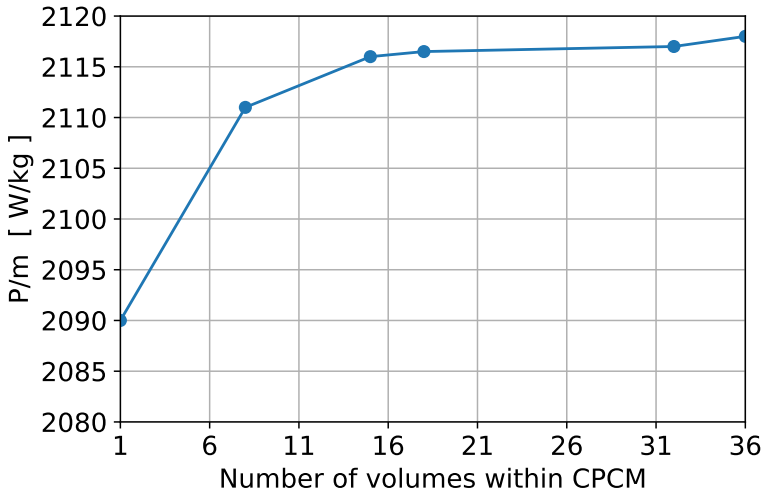

Figure 5.3. : Pareto curve showing the relationship between spatial discretization of the CPCM layer and the performance metric power per unit mass of the module for the extended plate HX.

5.2 Cylindrical Tube HX Geometry

In case of the cylindrical tube geometry, I consider three design variables: volume fraction of metal in the CPCM layer, ϕ, distributed spatially across the CPCM layer as shown in Figure 5.4, the thickness of the CPCM layer, t_c, and the length of the HX, L. To model a non-uniform distribution of metal fraction within the CPCM layer, I consider 18 volumes within the CPCM layer, each with its own metal fraction ϕ_i, as shown in Figure 5.4.

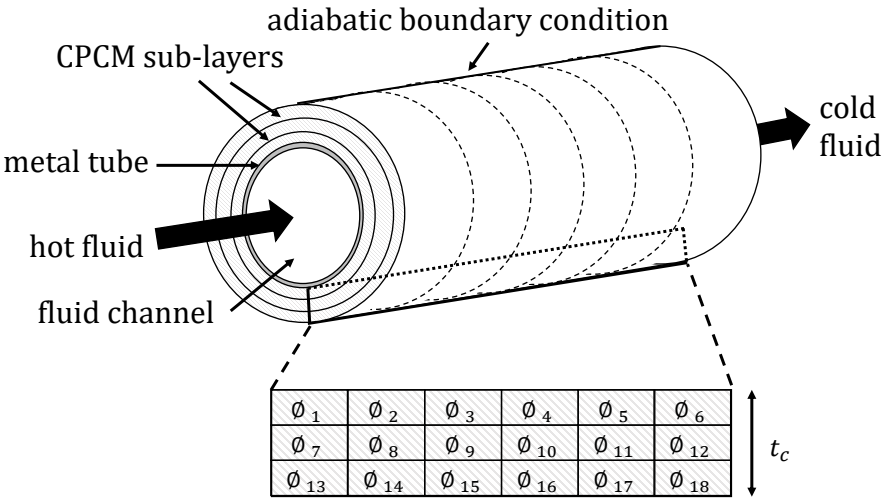

Figure 5.4. : Cylindrical tube HX with 18 volumes defined within the CPCM layer to be optimized.

All of the fixed parameters used to simulate the model at each iteration of the optimization are given in Table 5.3. The design optimization problem is defined in Equation 5.2 where $x_d = \begin{bmatrix} \phi_1 & \phi_2 & \dots & h_c & N \end{bmatrix}^T$ and $u = \begin{bmatrix} v_f & T_{in}^f & T(0) \end{bmatrix}^T$.

$$
\begin{aligned}
\min_{x_d} \quad & J\left(\boldsymbol{x_d}\right) = -\frac{\sum_{i=1}^{n_r n_L} m_{c,i} c_{p,i} \left(T_{c,i}\left(t_f\right) - T_{c,i}(0)\right) + \left(\sum_{i=1}^{n_r n_L} m_{c,i}\right) L_{fus}}{\pi L \left(\rho_c \left(r_c^2 - r_p^2\right) + \rho_f r_f^2 + \rho_p \left(r_p^2 - r_f^2\right)\right) t_f} \\
\text{s.t.} \quad & \pi L r_c^2 = 5 \times 10^{-4} \mathrm{m}^3 \\
& 0.01 \leq \phi_i \leq 0.99 \\
& 1 \text{ mm} \leq t_c \leq 15 \text{ mm} \\
& 10 \text{ cm} \leq L \leq 100 \text{ cm} \\
& \dot{x} = f(x_d, u)
\end{aligned}
\tag{5.2}
$$

Table 5.3. : List of fixed parameters used in the optimization case study.

Parameter	**Value**
simulated time (t_f)	10 s
time step (dt)	0.1 s
n_L	30
n_r	9
v_f	4 m/s
T_{in}	313.3 K
$T(0)$	303.3 K
T_m	303.3 K
t_p	1 mm
r_f	0.5 mm

The optimization problem is solved using the nonlinear optimization algorithm sequential quadratic programming (SQP) with multi-start, the same algorithm used in Section 5.1. The convergence tolerance on the cost function is 10^{-5} W/kg.

Again, similar to that in case of the extended plate HX, I quantify the benefit of a non-uniform spatial distribution of metal within the CPCM layer by comparing the results for the non-uniform case against the results of the case when the TES module is optimized with a uniform distribution of metal.

The optimal thickness of the CPCM layer, the optimal length of the HX, and the optimal value of average metal fraction by volume in the CPCM layer for the two cases are given in Table 5.4. The exact distribution of metal fraction by volume in percentage within the composite PCM layer for the case with non-uniform metal distribution is shown in Figure 5.5. The optimal distribution of metal fraction by volume within the CPCM layer is similar to that in case of the extended plate HX in the sense that, the first CPCM sub-layer has the highest metal fraction by volume, the second sub-layer has the second highest metal fraction by volume and the the third sub-layer has the least amount of metal. This is to maximize the rate of heat transfer in the radial direction away from the fluid flow to melt a large amount of PCM and

maximize the latent heat stored in the CPCM layer. The optimal distribution of metal fraction by volume within the CPCM layer for the cylindrical tube HX also shows that most of the metal is concentrated in the first sub-layer of the CPCM layer and the metal volume fraction in most of the volumes of the second sub-layer and in all the volumes of the third sub-layer is 0.01 which is the lower limit of the variable ϕ_i in the optimization problem. Since the area of contact between the first sub-layer and the second sub-layer of CPCM is lower than that between the second and the third sub-layers and the thermal conductivity is directly proportional to the area of contact, the optimal distribution of metal fraction is such that the effective thermal conductivity of the first sub-layer of CPCM is maximized as a results of a high volume fraction of metal in that layer.

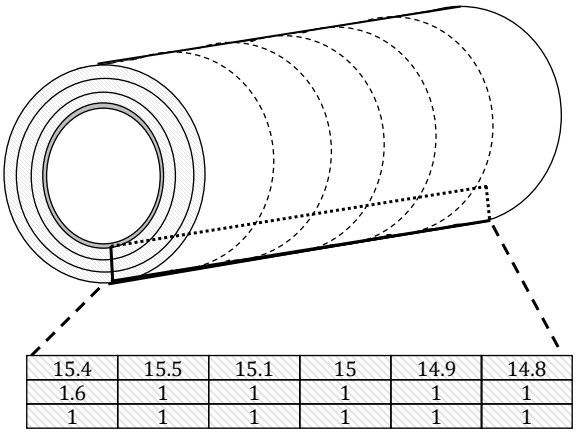

Figure 5.5. : Optimal metal distribution (in percent metal by volume) within the CPCM layer to maximize the power per unit volume performance measure.

Table 5.4. : Optimization results for uniform and non-uniform distribution of metal fraction by volume within the CPCM layer.

Variable	**Optimal Value** (Uniform Distribution)	**Optimal Value** (Non-uniform Distribution)
t_c	11.12 mm	11.12 mm
L	100 cm	100 cm
ϕ or $\bar{\phi}$	ϕ =6.4 %	$\bar{\phi}$ =5.7 %
P/m	155.29 W/kg	162.89 W/kg
P	123.56 W	126.55 W
m	795.6 g	776.9 g

Thus, by allowing for non-uniform spatial variation of the metal composition within the CPCM layer, the power per unit mass increased by 4.9% while the mass of the HX decreased by 1.5%, as compared to the case with metal distributed uniformly throughout the CPCM layer.

To check the sensitivity of the optimization results to the level of spatial discretization considered in the design problem, the optimization problem was solved for the same 6 cases used to create the Pareto curve in Section 5.1. The results are summarized in Figure 5.6 which characterizes the change in power per unit mass as a function of the level of spatial discretization of the metal within the CPCM layer. It is clear that the increase in spatial discretization increases the power per unit mass initially, but that the power per unit mass starts to saturate. Similar to the case of the extended plate HX, the Pareto curve shows that the performance metric starts to saturate at a certain number of volumes considered within the CPCM layer, and increasing the spatial discretization further would not improve the performance metric. Increasing the spatial discretization further would add complexity to the design problem without any contribution to the performance.

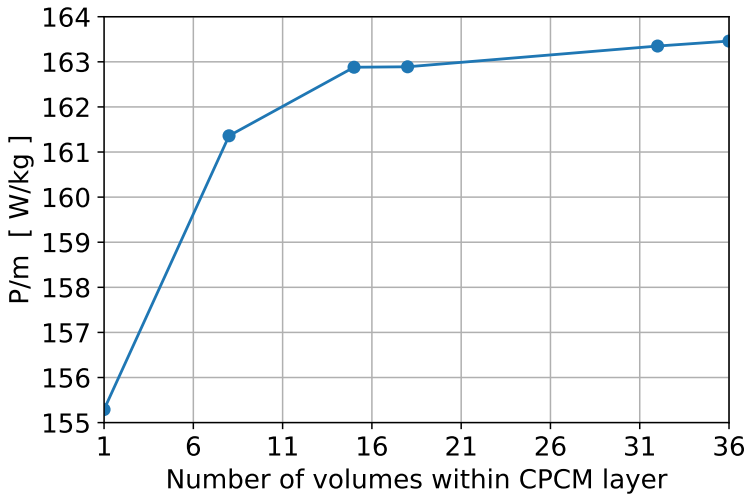

Figure 5.6. : Pareto curve showing the relationship between spatial discretization of the CPCM layer and the performance metric power per unit mass of the cylindrical tube HX.

The results of the design optimization case studies highlight the value of the reduced-order dynamic model for the purpose of design optimization. However, the specific numerical improvement in power per unit mass observed in the case studies may not necessarily be seen when the optimally designed modules are simulated and compared using a CFD software, due to the presence of error between the reduced-order model and the CFD model as discussed in Chapter 3. Moreover, the optimal metal volume fraction obtained in the case studies is below 10% which is difficult to manufacture while satisfying the assumption of metal fin spacing (< 1 mm). To that end, future design exploration must consider manufacturability constraints in the optimization itself. Nevertheless, the case studies presented here provide qualitative insight on the design process by suggesting that the effects of a non-uniform distribution of metal within the CPCM layer of a module are promising.

6. CONCLUSION

6.1 Summary of Research Contributions

In this thesis, I derived reduced-order (low fidelity) dynamic models for two geometric configurations of a metal-PCM composite HX. The reduced-order models were based on a finite-volume discretization approach with a lumped-parameter assumption applied to individual control volumes. The models were validated against a high fidelity CFD model developed in ANSYS Fluent for both laminar and turbulent flow regimes. I demonstrated the accuracy of the low fidelity models in predicting, both spatially and temporally, the evolution of the dynamic model states and other system variables of interest, such as PCM melt fraction. I then demonstrate parametric studies for both the extended plate HX and the cylindrical tube HX. The parametric case studies provided valuable insight as to the effects of the individual design variables on specific performance metrics of interest, but it is not a convenient method to conduct design optimization if the number of design parameters to be optimized is larger than 3. I then demonstrated how the reduced-order models could be used for the purposes of design optimization, with a large number of design parameters optimized simultaneously, by presenting case studies in which I maximized the power per unit mass of the overall TES module subject to a constraint on the volume occupied by the TES modules in a specified time interval. In the case of the extended plate HX geometry, the results showed that by allowing for non-uniform spatial variation of the metal within the CPCM layer, an optimal design was found that could achieve a 1.24% increase in performance with 0.4% less mass as compared to the case when the metal was uniformly distributed within the PCM layer. In the case of the cylindrical tube

HX, a 4.9% increase in performance with 1.5% less mass was achieved as compared to the case when the metal was uniformly distributed in these HXs. Importantly, the reduced-order models are suitable for design optimization of TES modules with any number of decision variables and a broad range of objective functions.

6.2 Future Work

There are several potential areas for future work that build on the contributions of this thesis. With respect to the module itself, a comprehensive uncertainty quantification between the reduced-order model and the high fidelity CFD model could be conducted to better understand the contribution of factors like Nusselt number correlations, spatial discretization of the module, and the effective composite properties assumption, among others, to the prediction error between the two models. To further quantify the accuracy of the reduced-order model, experimental data should be used to conduct a detailed validation. The proposed models could also be used to conduct a more comprehensive sensitivity study to quantify the effect of every design variable on performance metrics of interest, including varying the characteristics of the phase change material itself. A second area of future work concerns the manufacturability of the metal-PCM layer. The tradeoff between the increased manufacturing complexity of a module with spatial variation of metal within the PCM, versus the potential gains in performance, should be explored. Manufacturing methods, including additive manufacturing approaches, could also be studied in order to fabricate the types of modules proposed in this thesis. Finally, future work could consider the integration of the proposed TES module into a larger thermal-fluid system architecture. This would enable quantification of the performance benefits of the individual module in meeting system-level performance requirements. For integration with two-phase

cooling systems, future work will require revisions to the proposed models to consider two-phase flow through the fluid channel.

REFERENCES

REFERENCES

[1] Xiang-Qi Wang, Christopher Yap, and Arun S. Mujumdar. A parametric study of phase change material (PCM)-based heat sinks. *International Journal of Thermal Sciences*, 47(8):1055–1068, August 2008.

[2] S. F. Hosseinizadeh, F. L. Tan, and S. M. Moosania. Experimental and numerical studies on performance of PCM-based heat sink with different configurations of internal fins. *Applied Thermal Engineering*, 31(17):3827–3838, December 2011.

[3] R. Srikanth, Pavan Nemani, and C. Balaji. Multi-objective geometric optimization of a PCM based matrix type composite heat sink. *Applied Energy*, 156:703–714, October 2015.

[4] Ponnada Srivatsa, Rajesh Baby, and Chakravarthy Balaji. Geometric Optimization of a PCM-Based Heat Sink—A Coupled ANN and GA Approach. *Heat Transfer Engineering*, 37(10):875–888, July 2016.

[5] M. Lacroix. Numerical simulation of a shell-and-tube latent heat thermal energy storage unit. *Solar Energy*, 50(4):357–367, April 1993.

[6] Anica Trp, Kristian Lenic, and Bernard Frankovic. Analysis of the influence of operating conditions and geometric parameters on heat transfer in water-paraffin shell-and-tube latent thermal energy storage unit. *Applied Thermal Engineering*, 26(16):1830–1839, November 2006.

[7] Atul Nagose, Ankit Somani, Aviral Shrot, and Arunn Narasimhan. Genetic Algorithm Based Optimization of PCM Based Heat Sinks and Effect of Heat Sink Parameters on Operational Time. *Journal of Heat Transfer*, 130(1), January 2008.

[8] Y. B. Tao and Y. L. He. Numerical study on thermal energy storage performance of phase change material under non-steady-state inlet boundary. *Applied Energy*, 88(11):4172–4179, November 2011.

[9] Sujoy Kumar Saha and Pradip Dutta. Effect of melt convection on the optimum thermal design of heat sinks with phase change material. *Journal of Enhanced Heat Transfer*, 18(3):249–259, 2011.

[10] Y. B. Tao, Y. L. He, Y. K. Liu, and W. Q. Tao. Performance optimization of two-stage latent heat storage unit based on entransy theory. *International Journal of Heat and Mass Transfer*, 77:695–703, October 2014.

[11] R. Pakrouh, M. J. Hosseini, A. A. Ranjbar, and R. Bahrampoury. A numerical method for PCM-based pin fin heat sinks optimization. *Energy Conversion and Management*, 103:542–552, October 2015.

[12] M. Medrano, M. O. Yilmaz, M. Nogués, I. Martorell, Joan Roca, and Luisa F. Cabeza. Experimental evaluation of commercial heat exchangers for use as PCM thermal storage systems. *Applied Energy*, 86(10):2047–2055, October 2009.

[13] R. Srikanth and C. Balaji. Experimental investigation on the heat transfer performance of a PCM based pin fin heat sink with discrete heating. *International Journal of Thermal Sciences*, 111:188–203, January 2017.

[14] Patrick J. Shamberger and Timothy S. Fisher. Cooling power and characteristic times of composite heatsinks and insulants. *International Journal of Heat and Mass Transfer*, 117:1205–1215, 2018.

[15] V Shatikian, G Ziskind, and R Letan. Numerical investigation of a pcm-based heat sink with internal fins. *International Journal of Heat and Mass Transfer*, 48(17):3689–3706, 2005.

[16] Frank P. Incropera, Adrienne S. Lavine, Theodore L. Bergman, and David P. DeWitt. *Fundamentals of Heat and Mass Transfer*. Wiley, 2007.

[17] Stuart W. Churchill. Friction-factor equation spans all fluid-flow regimes. *Chemical Engineering*, 1977.

[18] Philippe Spalart and Steven Allmaras. A one-equation turbulence model for aerodynamic flows. In *30th Aerospace Sciences Meeting and Exhibit*, page 439, 1992.

[19] Vaughan R. Voller and C. Prakash. A fixed grid numerical modelling methodology for convection-diffusion mushy region phase-change problems. *International Journal of Heat and Mass Transfer*, 30(8):1709–1719, 1987.

[20] Paul T. Boggs and Jon W. Tolle. Sequential quadratic programming. *Acta Numerica*, 4:1–51, 1995.